Scientific Reports

https://doi.org/10.1038/s41598-026-49197-5

Article in Press

Precursory seismicity unveiled before the M_w7.1 Dingri earthquake in Tibet

Received: 24 September 2025

Accepted: 13 April 2026

Published online: 11 May 2026

Cite this article as: Pettenati F., Vuan A., Sandron D. *et al.* Precursory seismicity unveiled before the M_w7.1 Dingri earthquake in Tibet. *Sci Rep* (2026). https://doi.org/10.1038/s41598-026-49197-5

Franco Pettenati, Alessandro Vuan, Denis Sandron, Giampietro Verza & Matteo Picozzi

We are providing an unedited version of this manuscript to give early access to its findings. Before final publication, the manuscript will undergo further editing. Please note there may be errors present which affect the content, and all legal disclaimers apply.

If this paper is publishing under a Transparent Peer Review model then Peer Review reports will publish with the final article.

ARTICLE IN PRESS

© The Author(s) 2026. **Open Access** This article is licensed under a Creative Commons Attribution-NonCommercial-NoDerivatives 4.0 International License, which permits any non-commercial use, sharing, distribution and reproduction in any medium or format, as long as you give appropriate credit to the original author(s) and the source, provide a link to the Creative Commons licence, and indicate if you modified the licensed material. You do not have permission under this licence to share adapted material derived from this article or parts of it. The images or other third party material in this article are included in the article's Creative Commons licence, unless indicated otherwise in a credit line to the material. If material is not included in the article's Creative Commons licence and your intended use is not permitted by statutory regulation or exceeds the permitted use, you will need to obtain permission directly from the copyright holder. To view a copy of this licence, visit http://creativecommons.org/licenses/by-nc-nd/4.0/.

Precursory Seismicity Unveiled Before the Mw7.1 Dingri Earthquake in Tibet

Franco Pettenati[1], Alessandro Vuan[1,4], Denis Sandron[1], Giampietro Verza[2] and Matteo Picozzi[1,3]

[1] *Istituto Nazionale di Oceanografia e di Geofisica Sperimentale – OGS, Trieste, Borgo Grotta Gigante, 42/c 34010 Sgonico, Trieste, Italy,* [2] *EvK2CNR, Via San Bernardino, 145 24126 - Bergamo Italy* [3]*Università degli Studi di Napoli Federico II - Corso Umberto I 40 - 80138 Napoli, Italy,* [4]*Istituto Nazionale di Geofisica e Vulcanologia – INGV, Rome, Italy*

Correspondence and requests for materials should be addressed to D.S. (dsandron@ogs.it)

Abstract

On 7 January 2025, an Mw 7.1 normal-faulting earthquake struck the Dingri region in southwestern Xizang (Tibet), located within the extensional domain of the plateau - one of the most seismically active intraplate regions on Earth. Investigating the preparatory phase of such events in remote areas is particularly challenging due to limited station coverage. We analysed continuous records from IO.EVN, the only permanent seismic station within approximately 90 km of the epicentre that freely provides available data. Using an AI-based approach that integrates phase detection, polarisation analysis and template matching, we reconstructed an earthquake catalogue for the two years preceding the mainshock. Our results reveal a marked increase in event rate and clustering beginning about 45 days before the mainshock, coinciding temporally with an M_L 2.4 event at the Himalayan front. We interpret this evolution as a slow, progressive increase in seismicity, consistent with a late-stage nucleation process modulated by regional tectonics. Our results are therefore compatible with tectonic loading, and suggest that single-station seismic monitoring, when enhanced by AI techniques, can help identify retrospective seismicity patterns prior to rupture, even in data-sparse and tectonically complex regions.

Introduction

On 7 January 2025 an Mw7.1 normal-faulting earthquake (hereinafter referred to as the Dingri earthquake) occurred in southern Xizang (Tibet), Dingri County (Yao et al. 2025)[1] (Figure 1). The epicentre (28.57 N; 87.45 E) as reported by the China Earthquake Networks Centre (CENC)[1], was located 80 km northeast of Mount Everest (Fig. 1). Six km south of the world's highest mountain, there is an Italian Observatory (Pyramid), where a seismic station with a Güralp CMG-3ESPC (60 s) seismometer is also installed (IO.EVN)[2]. The IO.EVN seismic station was established eleven months before the Mw7.9 Gorkha earthquake in 2015 (orange triangle in Fig. 1) to improve seismic monitoring in a critical and poorly instrumented region near the border between Nepal and Tibet. IO.EVN is the only station in the epicentre region that provides free data to the scientific community for detecting and studying environmental vibrations (such as icequakes, avalanches, landslides) and natural seismicity[2]. Aware of limitations due to the use of a single seismic station, we apply a combination of AI-driven workflow seismic detection and the cross-correlation matching filter (see Methods section and Supplementary Material) to the continuous three-component seismic recordings from the IO.EVN station data. This enables the reconstruction of a detailed foreshock catalogue and the retrospective identification of long-term precursory signals leading to the mainshock. Previous studies on single-station analyses have shown that deep-learning approaches integrated with a supervised template matching can effectively reveal hidden or transient seismic signals[3].

The Tibetan Plateau is one of the most complex intracontinental regions with an active fault[4,5] due to the ongoing process of north-south convergence between India and Eurasia[6]. This ongoing convergence[7] at a rate of about 19±1.4 mm per year leads to compressive stresses, especially in the Himalayan region and along the border with Tibet. However, the simultaneous presence of normal and strike-slip fault systems indicates significant east–west extension within a complex structural configuration in the southern and central parts of Tibet[5-8]. GPS observations[9] show that the total extension rate of all rifts is about 18.4±1.7 mm per year^{-1}. This tectonic extensional regime generates large normal-fault earthquakes such as the Mw 7.1 Dingri earthquake.

Despite this complex configuration of faults, most crustal deformation is currently concentrated along the Himalayan arc and is driven by the high rate of convergence between the Indian and Eurasian plates. The rapid uplift of the plateau in the last 40 Ma (middle Palaeogene)[10] must also be considered for a clear overview of the deformation in this region. The Indo-Eurasian convergence is a puzzling geodynamic process that gives rise to several interpretative models[6]. All models propose that the Tibetan lithosphere is tectonically pushed eastward by the N-S convergence of the highly rigid Indian lithosphere, with eastern Tibet rotating clockwise[11]. Competing models of the Indo-Eurasian convergence, including gravitational collapse[12] and channel flow[13,14], instead emphasize the complex mechanical coupling and partial melting beneath southern Tibet. Recent geophysical studies[15,16], suggest a correlation between the locations of these channel flows and the Tibetan grabens.

Before examining the seismicity preceding the Mw 7.1 Dingri earthquake**,** we refer to data from the temporary seismic network installed by Yao et al. (2025)[1] and CENC in the epicentre area the day after the mainshock. Aftershocks indeed provide key constraints on the seismogenic source (see the black cloud in Fig. 2a) which can help us to retrospectively decipher the preparatory phase of the main Dingri earthquake. The spatial distribution of the aftershocks with 31,038 events from 8 to 19 January reveals a north-south structure divided by three main fault segments with different strike and dip directions. This fault belongs to one of the normal fault systems (Rift Systems[1,4]) that traverse the Tibetan plateau from south to north in a N–S direction on the northern edge of the Himalayas. Specifically, the fault is the Deng Me Cuo fault (hereafter DMCF)[1,5] part of the Shenzha-Dingjie rift system within the Xainza-Dingjie fault XDF (Fig. 1). The inversion of the InSAR data shows an average strike of 188°, a dip of 50° with a maximum displacement of 4-5 m and an average displacement angle of 83° at a depth of 5 km[9,17]. Another source inversion technique with multi-data integration[18], identified a three-fault system, coherent with[1], and estimated the centroid at a depth of 4,8 km, well constrained by seismic and geodetic data. This normal fault system with a length of ~15-50 km, coexists with a system of major strike-slip lines in the east-west direction. The processing of the InSAR data has shown that an east-dipping secondary fault is coseismically connected to the main fault[19].

The Dingri earthquake occurred in the region known as the Tethys Himalaya (Fig. 1), which borders the Yarlung Tsangbo Suture Zone (YSZ) to the north and the Great Himalayan Region to the south. The rift system, which includes the Dingri earthquake fault, intersects the South Tibetan Detachment System (STDS)[20], potentially limiting coseismic propagation. These observations support a tectonic setting where normal faulting in the Tibetan extensional domain interacts with inherited Himalayan structures (Fig. 1). The STDS is a series of low-angle faults with top-to-the-north shear zones that run parallel along the entire strike length (about 2000 km) of the Himalayan orogen and form the lower boundary of the Tethyan Himalayan sequence. Previous large normal-faulting earthquakes in Tibet, such as the Mw 7.1 Yutian event in 2008[21], demonstrate the potential for high-magnitude extensional ruptures in this intraplate region. The Mw 7.9 Gorkha thrust earthquake in 2015 also triggered aftershocks as far as southern Xizang[22]. These events highlight the need to assess possible stress interactions between the Himalayan front and normal faults within the plateau interior. One of them, occurred on 25 April 2015 at 09:17:03 UTC, with M_w 5.6 (Ms5.9)[22] (see Fig. 1), in the epicentre zone of the 2025 Dingri earthquake, and with a fault mechanism very similar to it (see the figure 1 in[22]). Fig. 2b shows the distribution of fault mechanisms in the GCMT catalogue (https://www.globalcmt.org/)[23], with predominantly normal faults (red), followed by strike-slip (blue) and reverse mechanisms (black) predominating in the Himalayan zone. The area A includes the circle of 70 km from epicentre visible in Fig. 2a. The most recent fault mechanism before the Dingri event occurred in 2021 (Fig. 2b).

The combination of AI-based detection, established single-station methods, and template matching enabled the reconstruction of a long-term record of the preparatory phase of a large intraplate earthquake in Tibet[24]. The observed pattern may be interpreted as consistent with a late-stage nucleation phase, potentially influenced by regional tectonics[25].

Methods and data analysis

From the perspective of a “single station”, we selected and localised the events using PhaseNet[26], a method based on a deep neural network (Supplementary Fig. S1). The description of the entire procedure can be found in the Supplementary material. We analyse the data from the IO.EVN station from 1 January 2023 to the time of the main earthquake 01:05:16.824 on 7 January 2025, and filtering between 2 – 8 Hz. All events clearly show that P arrivals and S-P travel times are within 14 s, indicating that these events are within approximately 120 km of the IO.EVN station. To calculate the distance, we checked the time synchronisation with the origin time from the high-resolution aftershock catalog[1] which provides P and S waves travel times (Supplementary Fig. S2). Finally, we used a polarisation analysis method[27] to calculate the azimuth. Thus, we obtained an initial catalogue of 289 events detected with PhaseNet[26] (hereinafter referred to as the “*template catalogue*”). For the detection of the complete catalogue of 1,138 events, we employed a supervised template matching (TM)[28,29], and used the 289 events as input templates. We refer to this catalogue as the "*augmented catalogue*". Because the analysis is based on a single seismic station, events detected through TM cannot be independently relocated. Therefore, all *augmented catalogue* events are assigned the location of the reference *template catalogue*. Figures 2, 3a-c, 4, 5, 8, and S2, S3 show only *template catalogue* events to highlight waveform families, while Figures 3d-e, 6, 7, 9, 10, and S7a-c use the full machine learning *augmented catalogue*. A full description of the procedures can be found in the Supplementary material.

Results

Spatial distribution of the aftershocks

Our backward analysis of the preparatory phase of the Mw 7.1 Dingri earthquake begins with the intriguing observation that the spatial distribution of the aftershocks from the Chinese dataset[1] suggests an excessive size relative to the moment magnitude, extending over nearly 100 km (see the black cloud in Fig. 2a). For a typical intraplate normal-faulting event with Mw 7.1, empirical scaling relations (e.g., Wells & Coppersmith, 1994[30]) predict a surface rupture length of ~40–50 km, with a maximum of about 60 km for the most recent relation of Thingbaijam et al. (2017)[31]. Although the actual source parametres are incomplete (e.g. stress drop), the aftershock cloud reflects a combination of rupture complexity[18,19], distributed slip, immature graben or stress transfer onto neighbouring structures, also in the light of studies on the seismic potential of crustal faults in Tibet[4]. Further studies are required to constrain the slip distribution and stress drop for this event, especially given the low density of seismological stations in the epicentral area.

Spatiotemporal distribution of the precursors

We show the location of the 289 events (*template catalogue*), detected exclusively by the IO.EVN station in Fig. 2a. The dataset covers the period from 1 January 2023 to the mainshock. These events were recognised by applying PhaseNet[26] and subsequently located through visual inspection on P and S phases and single station methods (see Methods section and the Supplementary). A significant number are concentrated within 70 km (red circle) around the mainshock[1] epicentre (yellow star). Two additional groups are observed: one to the south, in the Himalayan region, north-east of the Pyramid (white triangle), and the second forming a more scattered distribution towards the southeast, roughly following the Arun River valley. North of the epicentre, there is a gap in the data that probably coincides with the segment of the fault that underwent the main coseismic slip, as also suggested by InSAR data and modelling results shown in[18,19,32].

The 289 events are then used as templates identify smaller sibling earthquakes buried in the seismic noise by a template matching (TM) approach[33,34] (see Method and Supplement). Using TM, in the 2–8 Hz frequency band, we obtain a catalogue of 1,138 earthquakes (*augmented catalogue*), ranging from M-0.82 to M4.9, with a cross-correlation value ≥ 0.60 for all three available channels (Fig. 3d). All *augmented catalogue* events are plotted at the location of the reference *template catalogue* (see Methods).

The spatiotemporal evolution of foreshocks is often used to identify different stages of the preparatory phase and to investigate the potential effects of distant and delayed triggering in space and time[24]. We performed a non-parametric cumulative, interevent analysis in time (hours) and distance (km) of the *template catalogue* (Figs 3a,b). The temporal evolution of seismicity (bins in Fig. 3a) shows a sudden increase in the event rate about 40 days (990 hours, see the red arrow) This corresponds to a decrease in interevent time before the mainshock (triangles in Fig. 3a). The first detectable event within this phase is an M_L0.9 event of 27 November 2024 at 18:59:47, located about 74 km from the epicentre along the Himalayan margin 20 km east from Pyramid. This event may mark a transition in the seismicity pattern, although its physical role remains uncertain. In Fig. 3b, we observe two characteristic distances: the first discontinuity appears at ~30 km, while the second is at around 70 km from the mainshock. The temporal and spatial distributions shown in Figures 3a and 3b highlight two characteristic distance scales, approximately 30 km and 70 km from the epicentre. These distances seem to represent distinct physical processes occurring at different spatial scales. The 70 km radius encompasses most of the foreshocks recorded by the IO.EVN station and corresponds to the spatial extent of the extensional fault within the Shenzha-Dingjie rift system, as confirmed by the focal mechanisms in Fig. 2b. This greater distance likely defines a regional stress interaction zone, where long-range static stress changes or tectonic loading may influence seismicity. By contrast, the radius of approximately 30 km marks the internal nucleation zone, where a sharp increase in event frequency and momentum release is observed in the days preceding the mainshock (see Fig. 2a and 3c). At this stage, these distances do not indicate a specific physical mechanism, but they provide a useful framework for organising subsequent analyses. First, we focus on the larger spatial domain, and we analyse the cumulative magnitude-moment release for the two main seismic zones (Fig. 3c): i) within 70 km (red dots) from the epicentre, and ii) considering events beyond 70 km (blue dots). To convert the M_L of our catalogue in M_W, we used the relationship calibrated for the region[35]. In the Supplementary, we also provide Supplementary Fig. S3, where the analysis is repeated considering events within 30 km (red dots) and beyond (blue dots). The results for the two spatial scales do not appear to differ significantly, except for the density of the events in specific periods. The first increase in cumulative moment occurs within 70 km of the epicentre (red), due to the four events from 6 to10 April 2023 with a magnitude of 3.0 to 3.4, followed by three events in August with $M_L > 4.0$ (see 18 August 2023 M_L 4.3 in Fig. 2a). The sharp increase in the cumulative moment, beyond the 70 km (blue), is due to the event of 27 November 2023 M_L4.9 (Fig. 2a and Fig. S4a), which occurred 85 km east of the epicentre. This was followed by a period of low release and low event density within 70 km until the third decade of December, when on 28 December 2024 two M_L4.1 and 3.8 events occurred near the epicentre (Fig. 2a, and Fig. S4b), followed by the last foreshock of M4.4 one hour before the mainshock. These latter could explain the rapid upsurge of the cumulative moment shown in Fig. 3c. The gap period between 1 July and 1 October 2024 occurred mainly in the epicentral region, while only one significant M_L4.5 event occurred on 9 August 2024 in the Himalayan region east of the Pyramid (Fig. 2a). Fig. 3e shows the distribution over time of all *augmented catalogue* events in function of Mw. The events within 70 km appear to be organized into three clusters (red), with the last one preceding the mainshock by a few months. Events beyond 70 km (blue) show a concentration of low magnitude earthquakes during the months before the main event. Among them is the M_L0.9 event of 27 November 2024 belongs to this Himalayan cluster. As this event has a very low magnitude, it is not considered individually significant, but simply marks the early phase of the observed rate increase.

The first cluster began in the epicentral region during January-February 2023 (Fig. 3e) and developed roughly in an east-west direction. This is visible in Fig. 4a, the first snapshot of the spatiotemporal evolution of the precursors for the first dataset (*template catalogue*). It follows the course of the Pengqu River (Bumqu in Tibetan; see also Fig. 2a), which roughly corresponds to the position of the event cluster extending ESE-WNW in Fig. 2a south of the epicentre. Figure 4b shows the evolution from the April 2023 cluster to the end of 2023, with the second cluster consistently along the Pengqu River valley, a set of events around the epicentral valley, within the 30 km and some Mw>4 including the Mw 4.9 event of 27 November 2023. See also the cluster along the Arun River (see Fig. 2a). This was followed by the period of relative stasis in 2024 (01/01/2024–30/11/2024, Fig. 4c), and finally, in Fig. 4d, the final phase in December/January 2025 with the acceleration of foreshocks and the Mw > 3.8 events.

Analyses of seismicity for the complete catalogue

The b-value (i.e., the slope of the Gutenberg–Richter frequency–magnitude relationship, Gutenberg and Richter, 1942)[36] describes the relative ratio of small to large earthquakes. The interest in using this parameter to infer the preparatory phase is related to the observation that it is inversely related to the differential stress in the crust[37,38]. Therefore, temporal or spatial variations in the b-value have been interpreted as indicators of evolving stress regimes and are increasingly used to track preparatory processes that precede large earthquakes[33,39]. We opted for the b-positive (b+ hereafter) version[40], which is more robust than b-value that extrapolates magnitude completeness. As done before, we calculate b+ considering the two spatial scales identified (i.e., threshold distances) from the Dingri epicentre, applied to all detected events: earthquakes within 30 km (Figs 5a,b), using 526 events and beyond 30 km; (Figs 5c,d) events within 70 km (Figs 5e,f), with 993 events and beyond 70 km (Figs 5g,h). Both datasets allow robust estimates of the b+ (see e.g., Marzocchi et al 2019)[41]. For instance, in a recent article[42], the authors used a number equal to 150. The threshold value of 30 km has proven in this case to be more reliable as the b+ value remains stable as a function of ΔMc (differences in the order of magnitude of completeness). Furthermore, the b+ value for earthquakes within 30 km is quite high ~ equal to 1.2, while above this threshold it is stable at 0.7. The b+ value within the 70 km threshold is initially around 0.7 but less stable for different ΔMc (i.e., a clear drift appears for ΔMc > 0.3). This instability in b+ for the events within this wider range, which extends beyond the main fault, may indicate that the event population is heterogeneous. As shown in Fig. 2a, this region includes seismicity from the Himalayan front, potentially reducing reliability of the b+ estimate. Outside this area, the events are mainly distributed in the Himalaya and Nepal regions.

Discussion

Figure 4 show that in 2023, the seismicity was concentrated in the DMCF, with a spread of earthquakes, including those with M_L>4. The Figure 3e confirms this distribution, showing two clusters within 30 km at the beginning and end of the year. In 2024, after a period of relative calm and events distributed across the region, a cluster formed approximately 30 km southwest of the epicentre. In percentage terms, the cluster in Fig. 3e comprises: the first cluster, 8%; the second cluster of 2023, 16%; and the final cluster, 12% of the 1,138 events.

Figure 4d shows the final acceleration phase, with three events of $M_L>4$; the largest occurring 50 minutes before the mainshock.

In addition to the b-value analysis, the 30-km threshold is also useful for examining the evolution of seismicity. The cumulative seismic moment (Fig. 3c) shows a marked acceleration during the final phase preceding the mainshock, coinciding with a decrease in the b+ value outside the 30-km threshold. This temporal correspondence suggests that changes in the magnitude distribution accompany the accelerating phase of seismic release. However, we emphasise that the evolution of the b-value alone does not independently demonstrate a precursory activation process; rather, it must be interpreted alongside the cumulative moment release and clustering analyses. The temporal distribution of magnitudes (Fig. 3e) for events occurring ‘within’ and ‘beyond’ the epicentral area, shows that the events within 70 km are temporally clustered - specifically at the beginning of 2023, at the end of 2023, and again between late 2024 and early 2025, when the mainshock occurred - whereas events occurring between these clusters appear more scattered over time. The lower b+ outside the 30 km threshold (~0.7 – Figs5c,d) is consistent with seismicity occurring in regions of higher crustal strength. Conversely, we observe higher b+ in the epicentral area (~ 1.2 – Figs 5a,b) indicating a relative enrichment in small-magnitude events. At first glance, this result may appear counterintuitive, as it is often assumed that crustal stress is higher in the nucleation area than elsewhere. Such behaviour observed in the epicentral area may reflect enhanced crustal fracturing, either pre-existing or induced by a progressive weakening process, and/or the presence of crustal fluids (i.e. both conditions would lead to an increase in small earthquakes due to a progressive decrease in the shear resistance of the crust). Independent geophysical observations in the Dingri area indicate a mechanically weak crustal domain and complex stress perturbations during the earthquake cycle[43], providing a plausible physical framework for this weakening. Given that our analysis relies on data from only one seismic station operating in the area before the earthquake, we are currently unable to advance our interpretations further. However, future studies, facilitated by the recent deployment of additional seismic stations, are expected to yield deeper insights into the preparatory processes of large earthquakes in the Himalayan and Tibetan region.

Anyway, elevated b+ in epicentral area is consistent with models of Accelerating Moment Release (AMR) process[44]. As a precursor analysis, in Fig. 6a we show the fitting of a simple exponential model (1) as described by Mignan (2014)[45], as a simplified representation of the accelerating release of moment. This follows the formulation often used in precursor studies[46] although the author shows that this model has lost validity over time and discussed it critically in[44,47]. We used the formula, with the complete catalogue, for the last 3000 hours of the sequence, of *augmented catalogue*, long before the temporal variation of seismicity shown in Fig. 6a

$$N(t) = N_0 + Ae^{\beta t} \quad (1)$$

The positive β with a value of $9.1\ 10^{-4}$ and the good fit suggest that the final phase in the last 1000 hours (see the rise in the curve) clearly follows an exponential acceleration overall, which is consistent with a late-stage nucleation phase.

For the analysis with distance r, we used an inverse spatial Omori-law[47] (Fig. 6b)

$$N(r) = a\, r^{-\gamma} \quad (2)$$

The best-fitting exponent is $|\gamma| = 1.43 \pm 0.12$. The absolute value, being less than 2, indicates that the seismicity is not homogeneously distributed over a two-dimensional area but is instead organised along a restricted, fault-controlled domain. While $|\gamma| = 1.43$ mainly reflects a spatial organisation controlled by faults (dimension $D < 2$), the combination of this non-uniform scale with the marked temporal acceleration (Fig. 3c) indicates that seismicity becomes increasingly confined within a narrow epicentral domain prior to failure.

Always with the *augmented catalogue* data, Fig. 7a show the closer clustering near the epicentre over time, according to the inverse Omori analysis of shock distances, while Fig. 7b presents the clustering in terms of azimuth (relative to the epicentre). Both figures display an increase in the number of events that began around 1,100 hours before the mainshock. Thus, we have ascertained that it belongs to a cluster in the Himalayan region starting about 45 days before the mainshock (Fig. 3e). Again, using the *augmented catalogue*, a cluster at 26 km from the mainshock, is noteworthy, starting with the event of 23 November 2024, 21:05:52 M_L 2.4 - 90 hours before the M_L0.9, southwest of the epicentre and repeating until about 200 hours earlier. It could be that this small event did not lead to a more important one, but it indicates the transition to an unstable acceleration phase and an emerging of foreshocks (as long as the events are clustered both in space and time). The green and yellow dots in Fig. 7c show their evolution together with the concentration of events around the epicentre in the last 500 hours. This evolution, although based on a limited number of events, is consistent with a localised acceleration that may indicate the onset of a nucleation phase [48]. However, full coalescence of clusters cannot be conclusively established from the available data and remains a working hypothesis consistent with the observed patterns.

In line with the analysis of Fig. 3c and Figs 7, we refine the inter-event analyses for all combinations, by first generating the matrix for each pair (i,j) for Δt and Δr (Fig. 8a), and also compare it with a version in which positions are randomly swapped to test the non-randomness of the phenomenon (Fig. 8b). The result highlights a net concentration of pairs with small Δt (closely spaced time points) and Δr (short distances), characterising the overall spatio-temporal clustering of the sequence, rather than a mainshock-centred convergence. In Fig. 8b, the density in Δr, is much more evenly distributed even for the short times, so that the spatial clustering disappears, suggesting that there is organisation in the data and that it is not a random process. The specific concentration towards the mainshock epicentre is assessed independently using the distance-to-mainshock evolution (Fig. 7a) and the cumulative moment acceleration (Fig. 3c). To support this hypothesis, a log-logistic[49] was constructed for the inter-event pairs (i,j) of Δt in the last 3000 hours (Fig. 9), whereby the model

$$N(\Delta t) = \frac{L}{1+\left(\frac{\Delta t}{t_o}\right)^{-k}} \qquad (3)$$

L is a normalisation parameter which indicates the total number of inter-event pairs, $k = 1.38$ is the slope, which indicates rapid and sigmoidal growth, while $t_0 = 333$ hours, is the inflection time of the curve, which corresponds approximately to the time of the time of the final acceleration, beginning a few days before the two M~4 events of 28 December 2024 (see Fig. 2a). The log-logistic model fits well and shows that the temporal accumulation exhibits a scalar behaviour typical of models with balanced critical phases - neither explosive nor pure cascade[50,51] - although there is no clear boundary between foreshock styles.

Our results are consistent with a critical nucleation pattern[25,45] in which part of the fault (the northern segment of the DMCF) has slowly accumulated stress to an unstable state, leading to the transition to the final unstable acceleration phase. A similar increase in seismicity, triggered by an M~4 event a few days before the mainshock, was also observed prior to the 2015 Gorkha earthquake (Mw7.9)[52]. In that case, an M5.2 earthquake occurred ~240 km northwest of the Gorkha epicentre and marked the onset of a significant foreshock sequence. Although the tectonic contexts differ - the older is a low-angle Himalayan thrust, while Dingri is an intraplate normal fault event - both cases show that small-to-moderate magnitude events can act as temporal markers of a transition to unstable faulting.

The three identified clusters are broadly consistent with the northeastern displacement of the Himalayan-Tibetan system, as shown by the rotation of the strain rate and GNSS velocity field[6], supporting the interpretation of an active extensional regime in this sector. The Tibetan Plateau is a region of diffuse intraplate deformation[5-7]. Our results suggest that even in such intraplate contexts – often considered less predictable - high-resolution monitoring of individual stations, combined with AI-assisted detection, can help identify retrospective signatures of fault weakening and nucleation.

Finally, it remains to be verified whether the proposed sequence of precursors is consistent with an intraplate earthquake such as the one in Dingri. Bouchon et al. (2013)[24] compare 31 sequences in both interplate and intraplate cases (their figures S15). This authors, normalised the cumulative number of events to the total number of events to emphasise temporal evolution regardless of the absolute seismicity rate. In the interplate case, the acceleration phase preceding the mainshock is remarkably robust, but less so in the intraplate case. In Dingri case (Fig. 3c), the development of the cumulative moment shows a strong acceleration in the last 15 days. In this case, Figure 10a shows the normalised cumulative evolution of our sequence starting from 2,500 hours (104 days) before the mainshock, for comparison with fig. 4 and S15 of reference[24] where the authors use 150 days. We used less than 150 days because the events in the days between August and September are sparse, making the first phase of about 50 days less relevant (see Supplementary Fig. S7a). Figure 10b shows the evolution over the past 15 days. This is very similar to Supplementary Fig. S7b when using only the data from the range 28.25–29.50 N, 86.50–87.75 E (about 30 km from the epicentre) for the last 15 days. These last two cumulative graphs closely resemble the intraplate stacks from the past few days, as shown in figure S15b[24]. This indicates that the intraplate seismic activity (foreshocks) has been concentrated in the epicentral area over the past 15 days. As our catalogue includes part of the Himalayan region (interplate) and part of the southern Tibetan plateau (intraplate), Figure 10c also presents the normalised cumulative evolution of our sequence for the Himalayan region only (27.25–28.25 N, 86.50–87.60 E), from day 104th (before the mainshock) to 27 November 2024 (18:59:47), the time of the M_L =0.9 event is used here solely as a temporal reference marking the beginning of the detectable rate increase. The evolution is entirely different from Fig. 10b and S7b and highlights the Himalayan cluster. Figure S7c, considering the data in coordinates (27.25-28.25 N, 86.50-87.60 E) also confirms the scarcity of events in the Himalayan area after the event of 27 November.

Anyway, there are some partial inconsistencies between our sequence and that of Bouchon et al. 2013[24]. In this article, the stacked cumulative number of foreshocks curves is compared with ETAS curves[53]. The aim of this analysis is to assess whether the observed sequence prior to the mainshock is compatible with a purely cascading random triggering model (ETAS) or whether it exhibits more structured behaviour. While the ETAS simulations reproduce final acceleration, it remains systematically weaker than that observed in the stacked cumulative curves. In contrast, no acceleration is seen in Figures 10a,b close to the mainshock. These results suggest that a simple cascading triggering model alone may not fully account for the observed acceleration. Instead, the data appear more consistent with a progressively organised phase of seismicity, although alternative explanations cannot be fully excluded. Furthermore, in[24] is reported that only 16% of the 31 intraplate sequences show the highest magnitude foreshock in the last eight hours, compared to 42% for interplate sequences. In our case, the highest magnitude foreshock of the final acceleration occurred 1 hour before the mainshock. This observation also agrees with that of Númez-Jara et al. (2025)[54] during the preparatory phase of large earthquakes in Turkey, supporting the broader relevance of precursor clustering, regardless of faulting style. However, to compare the intraplate sequence in the epicentral area with the sequence confined to the Himalayas, further analysis is required.

Conclusions

In this study, we analyse the long-term preparatory phase of the Dingri earthquake using a single-station AI-enhanced workflow. The resulting high-resolution catalogue in the two years before the mainshock reveals three clusters and highlights the capability of single station monitoring to detect seismic rate changes in complex intraplate settings such as Tibet. 45 days before the Mw7.1, the observed slow and progressive increase in seismicity rate, along with clustering within a ~30 km radius, is consistent with a late-stage nucleation process. Distance analysis also indicates a progressive acceleration, corresponding to the onset of a seismic cluster mainly in the third decade of December 2024, followed by two major M 4.0 events on 28 December, suggesting a possible organisation of foreshocks along a restricted, fault-controlled domain.

This acceleration in the cumulative seismic moment (Fig. 3c) and in the normalised stacking analysis (Fig. 10a) is spatially confined within 30 km of the epicentre. In the same region, we observe elevated b+ values (~1.2), indicating a relative increase of small-magnitude events. Although the evolution of the b-value alone does not independently demonstrate nucleation, this spatial and temporal correspondence is consistent with progressive microfracturing or heating in the middle-to-lower crust[14,43], that may have preceded instability. The b+ analysis therefore provides complementary support for the precursory activation rather than constituting standalone evidence.

The consistency between our results and the tectonic setting of the Tibetan Plateau – an intraplate region characterised by distributed deformation and high stress concentration due to India–Asia convergence supports the interpretation of an intraplate sequence in the epicentral area.

Further studies are needed to better understand the complex interaction between an interplate region (Himalayas) and an intraplate region (Tibet

Plateau). Integrating additional seismic stations would provide more accurate data on the processes preceding large earthquakes in this transition zone.

References

1. Yao, J., Yao, D., Chen, F., Zhi, M., Sun, L. & Wang D. A preliminary catalog of early aftershocks following the 7 January Mw 6.8 Dingri, Xizang earthquake. *J. Earth Sci.* XX, 1–15. https://doi.org/10.1007/s12583-025-0210-9 (2025).
2. Pettenati, F. et al. The seismic station IO.EVN at Pyramid EvK2CNR (Everest): 10 years of activity. *Seismol. Res. Lett.* 96, 1733–1746. https://doi.org/10.1785/0220240111 (2025).
3. Zali, Z., Mousavi, S. M., Ohrnberger, M., Eibl, E. P., & Cotton, F. Tremor clustering reveals pre-eruptive signals and evolution of the 2021 Geldingadalir eruption of the Fagradalsfjall Fires, Iceland. Communications Earth & Environment, 5(1), 1. (2024).
4. Li, Y. *et al.* Slip deficit rate and seismic potential on crustal faults in Tibet. *Geophys. Res. Lett.* 52, e2024GL112122. https://doi.org/10.1029/2024GL112122 (2025).
5. Wu, X. et al. The China Active Faults Database (CAFD) and its web system. *Earth Syst. Sci. Data* 16, 3391–3417. https://doi.org/10.5194/essd-16-3391-2024 (2024).
6. Pietrolungo, F. et al. Comparison of crustal stress and strain fields in the Himalaya–Tibet region: geodynamic implications. *Remote Sens.* 16, 4765. https://doi.org/10.3390/rs16244765 (2024).
7. Dal Zilio, L., van Dinther, Y., Gerya, T. & Avouac, J._P. Bimodal seismicity in the Himalaya controlled by fault friction and geometry. *Nat. Commun.* 10, 48. https://doi.org/10.1038/s41467-018-07874-8 (2019).
8. Armijo, R., Tapponnier, P., Mercier, J. L. & Han T.-L. Quaternary extension in southern Tibet: field observations and tectonic implications. *J. Geophys. Res. Solid Earth* 91, 13803–13872 (1986).
9. Liu, Q. et al. Geodetic observations and seismogenic structures of the 2025 Mw 7.0 Dingri earthquake: the largest normal faulting event in the southern Tibet Rift. *Remote Sens.* 17, 1096. https://doi.org/10.3390/rs17061096 (2025).

10. Rowley, D.B. & Currie, B. S. Palaeo-altimetry of the Late Eocene to Miocene Lunpola Basin, central Tibet. *Nature* 439, 677–681 (2006).

11. Tapponnier, P. & Molnar, P. Slip-line field theory and large-scale continental tectonics. *Nature* 264, 319–324 (1976).

12 Molnar, P. & Tapponnier, P. Active tectonics of Tibet, *J. geophys. Res.*, **83**, 5361–5376. (1978).

13. Li, S. et al. Partial melt or aqueous fluid in the mid-crust of southern Tibet? Constraints from INDEPTH magnetotelluric data. *Geoph. J. Int.*, *153*(2), 289–304. https://doi.org/10.1046/j.1365-246x.2003.01850.x. (2003).

14. Li D, Tian X, Liang X, Nie S. Different Formation Modes of the North–South-Trending Rifts in Southern Tibet: Implications From Ambient Noise Tomography. *Geophysical Research Letters* **51**, https://doi.org/10.1029/2024GL108254 (2024).

15. Hetenyi, G., Verne, J., Bollinger, L. & Cattin, R. Discontinuous low-velocity zones in southern Tibet question the viability of the channel flow model. *Geological Society*, *353*(1), 99–108. https://doi.org/10.1144/sp353.6. (2011).

16 Bischoff SH, Flesch LM. Normal faulting and viscous buckling in the Tibetan Plateau induced by a weak lower crust. *Nature Communications* **9**, 4952 https:// doi.org10.1038/s41467-018-07312-9 (2018).

17. Yu, S., Zhang, S., Luo, J., Li, Z. & Ding, J. The tectonic significance of the Mw 7.1 earthquake source model in Tibet 2025 constrained by InSAR data. *Remote Sens.* 17, 936. https://doi.org/10.3390/rs17050936. (2025).

18. Zhao, X., Xiao, Z., Wang, W., & Li, J. Along-strike variation of the unilateral rupture of the 2025 *M*w7.1 Dingri, Xizang earthquake: One of the shallowest M7+ normal-faulting events on
the Tibetan Plateau. *Geophysical Research Letters*, *52*, e2025GL119397. https://doi.org/10.1029/2025GL119397 (2025).

19. Qiao, X. *et al*. The 2025 M_W7.0 Dingri earthquake: Conjugate normal faulting of a graben structure in the southern Xainza-Dinggye rift. *Geophys. Res. Letters*, *52*, e2025GL116154. https://doi.org/10.1029/2025GL116154. (2025).

20. Kellett, D. A., Cottle, J. & Larson, K. P. The South Tibetan Detachment System: history, advances, definition and future directions. *Geol. Soc. Lond. Spec. Publ.* 483, 377–400 (2019).

21. Elliott, J.R. et al. Extension on the Tibetan Plateau: recent normal faulting measured by InSAR and body wave seismology. *Geophys. J. Int.* 183, 503–535. https://doi.org/10.1111/j.1365-246X.2010.04754.x. (2010).

22. Liu, C., Dong, P. & Shi, Y. Stress change from the 2015 Mw 7.8 Gorkha earthquake and increased hazard in the southern Tibetan Plateau. *Phys. Earth Plan. Int.* 267, 1–8, http://dx.doi.org/10.1016/j.pepi.2017.04.002. (2017).

23. Ekström, G. Nettles, G. M. & Dziewonski, A. M. The global CMT project 2004-2010: Centroid-moment tensors for 13,017 earthquakes, *Phys. Earth Planet. Inter.*, 200-201, 1-9, doi:10.1016/j.pepi.2012.04.002. (2012).

24. Bouchon, M, Durand, V., Marsan, D., Karabulut, H. & Scmittbuhl, J. The long precursory phase of most large interplate earthquakes. *Nat. Geosci*. 6, 299–302. https://doi.org/10.1038/ngeo1770. (2013).

25. Dieterich, J. H. Earthquake nucleation on faults with rate- and state-dependent strength. *Tectonophysics* 211, 115–134 (1992).

26. Zhu, W. & Beroza, G.C. PhaseNet: a deep-neural-network-based seismic arrival-time picking method. *Geophys. J. Int.* 216, 261–273. https://doi.org/10.1093/gji/ggy423. (2019).

27. Vidale, J.E. Complex polarization analysis of particle motion. *Bull. Seismol. Soc. Am.* 76, 1393–1405 (1986).

28. Montalbetti, J.F. and Kanasewich, E. R. Enhancement of teleseismic body phases with a polarization filter. *Geophys J Int*, 21(2), 119-129. (1970).

29. Liu, M., Zhang, M., Zhu, W., Ellsworth, W. L. & Li, H. Rapid characterization of the July 2019 Ridgecrest, California, earthquake sequence from raw seismic data using machine-learning phase picker. *Geophys Res Lett* 47. https://doi.org/10.1029/2019GL086189. (2020).

30. Wells, D. L. & Coppersmith, K. J. New empirical relationships among magnitude, rupture length, rupture width, rupture area, and surface displacement. *Bull. Seismol. Soc. Am.* 84, 974–1002. (1994).

31. Thingbaijam, K. K. S., Mai, P. M. & Goda, K. New empirical earthquake source-scaling laws. *Bull. Seismol. Soc. Am.*, 107(5), 2225–2246. https://doi.org/10.1785/0120170017. (2017).

32. Chen, A. *et al.* InSAR Reveals Coseismic Deformation and Coulomb Stress Changes of the 2025 Tingri Earthquake: Implications for Regional Hazard

Assessment. ISPRS Int. *J. Geo-Inf.*, 14, 430. https://doi.org/10.3390/ijgi14110430. 2025

33. Vuan, A., Sugan, M. Amati, G. & Kato, A. Improving the Detection of Low-Magnitude Seismicity Preceding the Mw 6.3 L'Aquila Earthquake: Development of a Scalable Code Based on the Cross Correlation of Template Earthquakes. *Bull. Seism. Soc. Am*, 108 (1): 471–480. doi: https://doi.org/10.1785/0120170106. (2018).
34. Sugan, M., Campanella, S., Chiaraluce, L., Michele, M & Vuan, A. The unlocking process leading to the 2016 Central Italy seismic sequence. *Geophys. Res. Lett.*, 50, e2022GL101838. https://doi.org/10.1029/2022GL101838. (2023).
35. Tang, C.-C., Zhu, L. & Huang, R. Empirical Mw–ML, mb, and Ms conversions in western China. *Bull. Seismol. Soc. Am.* 106, 2614–2623. https://doi.org/10.1785/0120160148. (2016).
36. Gutenberg, B. & Richter, C.F. Earthquake magnitude, intensity, energy and acceleration. *Bull. Seism. Soc. Am*, 32, 163-191. (1942)
37. Tormann, T., Wiemer, S., & Hardebeck, J. L. Earthquake recurrence model fail when earthquake fail to reset the stress field. *Geophys. Res. Lett.* 39, 1-6. https://doi.org/10.1029/2012GL052913. (2012).
38. Scholz C.H. On the stress dependence of the earthquake b value. *Geophys. Res. Lett.* 42, 1399–1402, https://doi.org/10.1002/2014GL062863. (2015).
39. Picozzi, M., Iaccarino, A. G. & Spallarossa D. The preparatory process of the 2023 Mw 7.8 Türkiye earthquake. Scientific Reports, 13:17853, 1-10, https://doi.org/10.1038/s41598-023-45073-8. (2023).
40. van der Elst, N. J. B-positive: a robust estimator of aftershock magnitude distribution in transiently incomplete catalogs. *J. Geophys. Res. Solid Earth* 126, e2020JB021027. https://doi.org/10.1029/2020JB021027. (2021).
41. Marzocchi, W., Spassiani, I., Stallonei, D, A. & Taroni, M. How to be fooled searching for significant variations of the b-value. Geophys. J. Int., 220, 1845–1856, doi:10.1093/gji/ggz541. (2019).
42. Dresen, G., Kwiatek, G., Goebel, T. & Ben-Zion, Y. Seismic and Aseismic Preparatory Processes Before Large Stick–Slip Failure. Pure Appl. Geophys., 177, 5741–5760, doi:10.1007/s00024-020-02605-x. (2020).

43 Ma, Z., Li, C., Zeng, H. et al. Deciphering stress perturbations throughout the 2025 Mw 7.1 Dingri, Southern Xizang Earthquake. *Nat Commun* (2025). https://doi.org/10.1038/ s41467-025-68128-y

44. Mignan, A. Non-Critical Precursory Accelerating Seismicity Theory (NC PAST) and limits of the power-law fit methodology. *Tectonophysics* 452 42–50 (2008). https://doi.org/10.1016/j.tecto.2008.02.010 . (2008).

45. Mignan, A. The debate on the prognostic value of earthquake foreshocks: a meta-analysis. *Sci. Rep.* 4, 4099. https://doi.org/10.1038/srep04099. (2014).

46. Bufe, C.G. & Varnes, D.J. Predictive modeling of the seismic cycle of the greater San
Francisco Bat region. *J. Geophys. Res.* 98, 9871–9883. (1993).

47. Mignan, A. Retrospective on the Accelerating Seismic Release (ASR) hypothesis: Controversy and new horizons. *Tectonophysics* 505. 1–16. https://doi.org/10.1016/j.tecto.2011.03.010. (2011).

48. Ben-Zion, Y. & Zaliapin, I. Localization and coalescence of seismicity before large earthquakes. *Geoph. J. Int.* 223, 1, 561-583. https://doi.org/10.1093/gji/ggaa315. (2020).

49. Ley, C., & Simone, R. Modelling Earthquakes: Characterizing Magnitudes and Inter-Arrival Times. In A. Bekker et al. (Eds.), *Computational and Methodological Statistics and Biostatistics* (pp. 29–50). Springer. https://doi.org/10.1007/978-3-030-42196-0_2. (2020).

50. Helmestetter, A. & Sornette, D. Foreshocks explained by cascades of triggered
Seismicity. *J. Geophys. Res.*108, NO. B10, 2457, 1-10, doi:10.1029/2003JB002409. (2003)

51. Marsan, D. & Lengliné, O. Extending earthquakes' reach through cascading. *Science 319,* 21 1076–1079. https://doi.org/10.1126/science.1148783. (2008).

52. Huang, H. et al. Matched-filter detection of the missing pre-mainshock events and aftershocks in the 2015 Gorkha, Nepal earthquake sequence. *Tectonophysics* 714, 71–81 (2017).

53. Ogata, Y. Statistical models for earthquake occurrence and residual analysis for
point processes. J. Am. Stat. Assoc. 83, 9_27 (1988).

54. Núnez-Jara, S. et al. Unraveling the spatiotemporal fault activation in a complex fault system: the run-up to the 2023 MW 7.8 Kahramanmaras¸ earthquake, Türkiye. *Earth Planet. Sci Lett.*, 669, 119570, 1-13, https://doi.org/10.1016/j.epsl.2025.119570. (2025)
55. Peng, Z. & Zhao, P. Migration of early aftershocks following the 2004 Parkfield earthquake. *Nature Geoscience* 2, 877–881 https://doi.org/10.1038/ngeo697. (2009).
56. Vuan, A., et al. Intermittent slip along the Alto Tiberina low-angle normal fault in central Italy. *Geophys. Res. Lett.*, 47, e2020GL089039. https://doi.org/10.1029/2020GL089039. (2020).

Acknowledgements

We thank Riccardo Percacci for help in the initial phase of data analysis.

Author contributions

F.P., A.V. D.S. and M.P. provided research idea. F.P. analysed all events detected by PhaseNet, performed the models of interevent analysis and wrote the paper. A.V. performed the PhaseNet analyses and filter matching detections and wrote the test of methods in the Supplement. D.S. contributed with the calculation and compilation of the catalogue. M.P. contributed with seismicity analyses. G.P involved in data acquisition and maintaining the IO.EVN broadband station. All authors took part in finalizing the manuscript.

Data availability

Data within the manuscript and its Supplementary Information are available from
the corresponding author upon reasonable request.

Competing interests: The authors declare no competing interests.

Funding: Not applicable

Additional information

Supplementary Information accompanies this paper at ….

Captions

Fig. 1 Simplified tectonic map of eastern Nepal and the southern part of the Tibetan plateau, with the most important tectonic features. The largest star marks the epicentre of 7 January 2025 a Mw7.1 Dingri earthquake southestern Xizang (Tibet), the yellow triangle indicates the location of the Pyramid Laboratory/Observatory, which is about 6 km from Mount Everest. The small star near the Dingri earthquake is the M_L5.6 of 25 April 2015 (epicentre EMSC-CSEM - https://www.emsc-csem.org/), aftershock of the Gorkha M_w7.9 earthquake, whose epicentre is the small star to the west of the other two.

Fig. 2a Map of the 289 events (*template catalogue*) identified by PhaseNet. The white triangle marks the location of the EvK2cnr pyramid, where the IO.EVN (OGS) seismic station is installed. The yellow star indicates the epicentre

(CENC catalogue) of 7 January 2025 a Mw7.1 Dingri earthquake, and the black dotted cloud shows the distribution of aftershock from their catalogue. The larger red circle encompasses events within 70 km of the epicentre, while the smaller circle includes those within 30 km.

Fig 2b Distribution of fault mechanisms of the GCMT catalogue (https://www.globalcmt.org/) (1980-2025): normal faults (red), strike-slip (blue) and reverse mechanisms (black) in the Himalayan zone. We distinguish three zone in which normal faults predominant. Zone A is the area of the Dingri earthquake epicentre and the events that are more directly related to the Dingri earthquake and are the subject of the analyses proposed in this study. Zone A corresponds to the area within the large red circle of Fig. 2a. B and C Zones where normal mechanisms prevail, but north of the epicentre. Zone D is the area of Mw/.8 Gorkha earthquake of 25 April 2015.

Fig. 3 a) Non-parametric cumulative analysis in time of the zone A (Figs 2) of *template catalogue* events; **b)** non-parametric cumulative interevent analysis in distance of the zone A (*template catalogue*); **c)** development of the cumulative moment release (*template catalogue*) with a radius of 70 km around the epicentre of the Dingri earthquake (within 70 km red dots, beyond 70 km blue dots); **d)** histograms comparing the magnitude of 289 (*template catalogue*) events (brown) with the complete data set of 1,138 (*augmented catalogue*) events (blue); **e)**. Mw distribution of all 1,138 events over time: (within 70 km red dots, beyond 70 km blue dots). The red arrow in Fig. 3a indicates the temporal position of M_L0.9 event of 27 November 2024 at 18:59:47. The red arrow in Fig. 3b indicates the start of the final acceleration beginning with the epicentral cluster at the end of December.

Fig. 4 Four different periods in the evolution of (*template catalogue*) events before the Dingri earthquake; **a)** snapshot of period 01/01/2023 – 10/04/2023: **b)** period 11/01/2023 – 31/12/2023; **c)** period 01/01/2024 - 30/11/2024; **d)** period 01/12/2024 a 07/01/2025. The yellow star marks the epicentre of Dingri earthquake, the triangle indicates the location of the Pyramid

Laboratory/Observatory and the IO.EVN station. The figures report the relevant events with Mw > 4.

Fig. 5 Seismicity analyses (*template catalogue*) according to b-positive in two window thresholds: **a-b)** within 30 km; **c-d)** outside 30 km; **e-f)** within 70 km; **g-h)** outside 70 km. Above the Gutenberg–Richter analysis with the histograms of Δ-magnitude; below the analyses of the stability of the b-positive in function of ΔMc magnitude of completeness.

Fig. 6 *augmented catalogue* data: **a)** Fitness of the model Accelerating Moment Release (AMR) model[44], formula (1) of the last 3000 hours of the complete dataset of events within zone A of Figs 2. Blue is the cumulative number of events, and the red dashed curve is the fitted model; **b)** Fitness of the model of inverse spatial Omori[47], formula (2) of the last 3000 hours the complete dataset of events within zone A. Blue is the cumulative number of events, and the red dashed curve is the fitted model.

Fig. *augmented catalogue* data: **7 a)** Temporal evolution in distance with respect to the epicentre; **b)** temporal evolution in azimuth with respect to the epicentre. You can see the increase in the number of events in the last 1000 hours before the main earthquake. **c)** polar diagrams in the development of the last 1500 hours before the main earthquake. The colours in the legend represent the cumulative number of events in the same position.

Fig. 8 *augmented catalogue* data: **a)** matrix of the inter-event analysis based of all combinations for each pair (i,j) for Δt and Δr of the entire dataset; **b)** matrix of the randomly swapped positions version pairs (i,j) for Δt and Δr, for comparison with empirical matrix a).

Fig. 9 Fitness of the log-logistic[49] for the inter-event pairs (i,j) (*augmented catalogue*) of Δt over the last 3000 hours, using the model (3). t_0 indicates the inflection time of the curve when the final critical phase begins.

Fig. 10 Normalized cumulative evolution of the events using the *augmented catalogue* data (red), before the intraplate Dingri earthquake of 7 January 2025, Mw7.1. The blue curves show the corresponding ETAS sequence simulation. **a)** the normalized evolution starting from 2500 hours (104 day) before the main shock; **b)** the normalized evolution in the last 15 days; **c)** normalized evolution of our sequence for the Himalayan region only (27.25-28.25 N, 86.50-87.60 E), from the 104th day to the M_L0.9 27 November 2014 (18:59:47) event.

Supplementary Fig. S1 100 Hz three component signals recorded on 7th January 2025. Dotted lines indicate P and S picks (blue and orange, respectively) obtained by PhaseNET. Red dotted lines correspond to the origin times of the Chinese catalogue.

Supplementary Fig. S2 P and S observed correspond to aftershocks in the time range from 2025-01-08 to 2025-01-19 determined by the local network in China. Dots correspond to P (blue) and S (yellow) retrieved by PhaseNET on EVN station have a reliable origin time for EVN.

Supplementary Fig. S3 Temporal development of the cumulative moment release with *template catalogue* events, within 30 km (red dots) and beyond 30 km (blue dots), from the epicentre of Dingri earthquake

Supplementary Fig. S4 Three component seismograms of four aftershocks detected by PhaseNet19. **a)** 27/11/2023 - 22:16:03 M_L4.9; **b)** 28/12/2024 - 06:05:58 M_L4.1.

Supplementary Fig. S5 Histograms of scores for phase type P and S. We filtered out score values lower than 0.8 and 07 for P and S phases, respectively.

Supplementary Fig. S6 Polarization analysis for the event 2nd January 2025 at 01:38:20 UTC. The panels show the raw three component data. After removing the instrument, we obtain the backazimuth, and incidence angles, together with rectilinearity, planarity and ellipticity values.

Supplementary Fig. S7 *augmented catalogue* data: Normalized stack evolution of the events in the catalougue of 1,138 data, before the intraplate Dingri earthquake of 7 January 2025, Mw7.1. The blue curves show the corresponding ETAS sequence simulation. **a)** the normalized evolution starting from 150 days before the mainshock; **b)** normalized evolution using data from the range 28.25-29.50 N, 86.50-87.75 E (about 30 km from the epicentre) for the last 15 days; **c)** normalized evolution for all 104 days for the Himalayan region (27.25-28.25 N, 86.50-87.60 E).

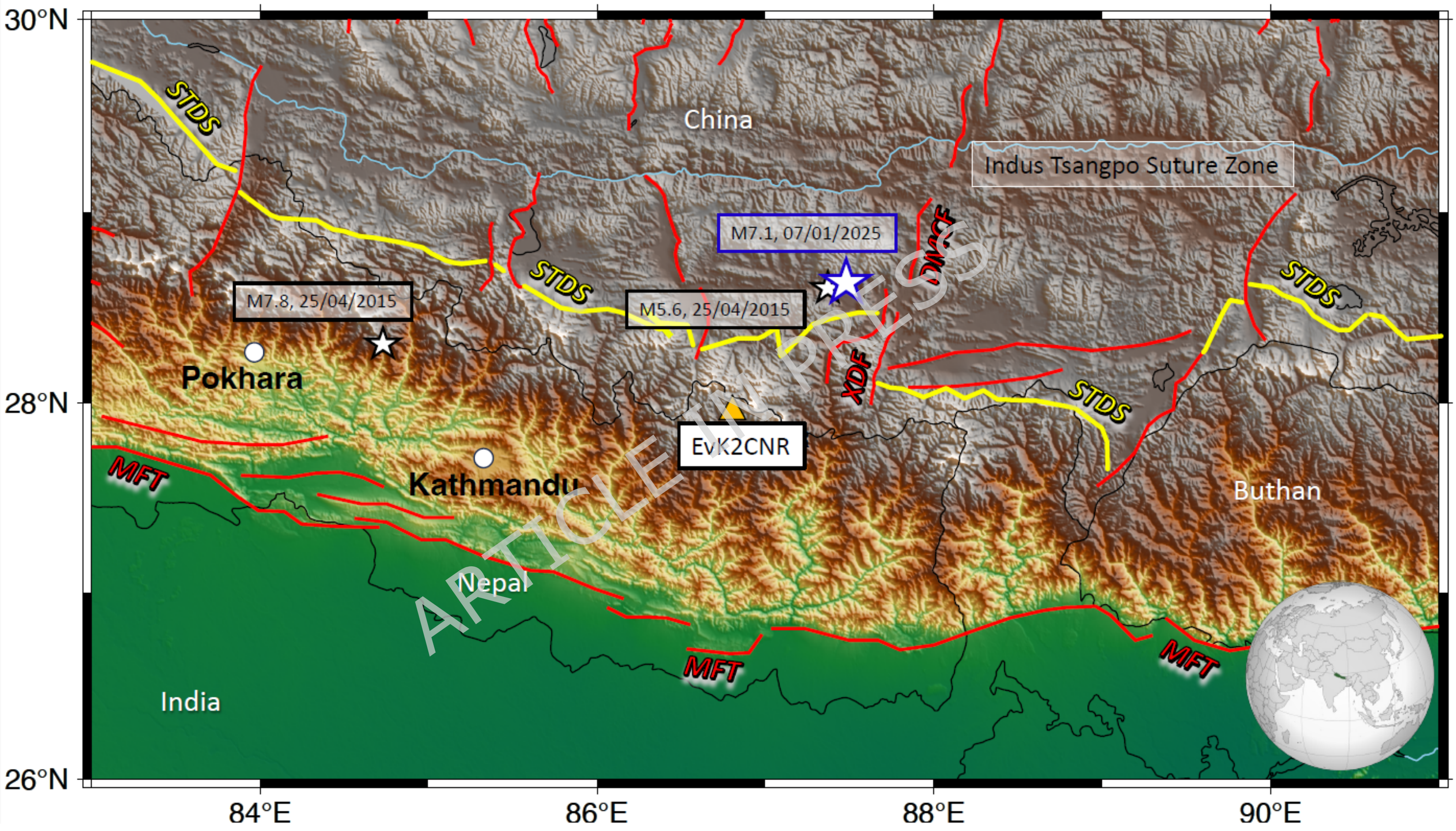
30°N
28°N
26°N
84°E
86°E
88°E
90°E
China
Indus Tsangpo Suture Zone
STDS
STDS
STDS
STDS
M7.1, 07/01/2025
DMCF
XDF
M7.8, 25/04/2015
M5.6, 25/04/2015
Pokhara
Kathmandu
EvK2CNR
MFT
MFT
MFT
Nepal
India
Buthan

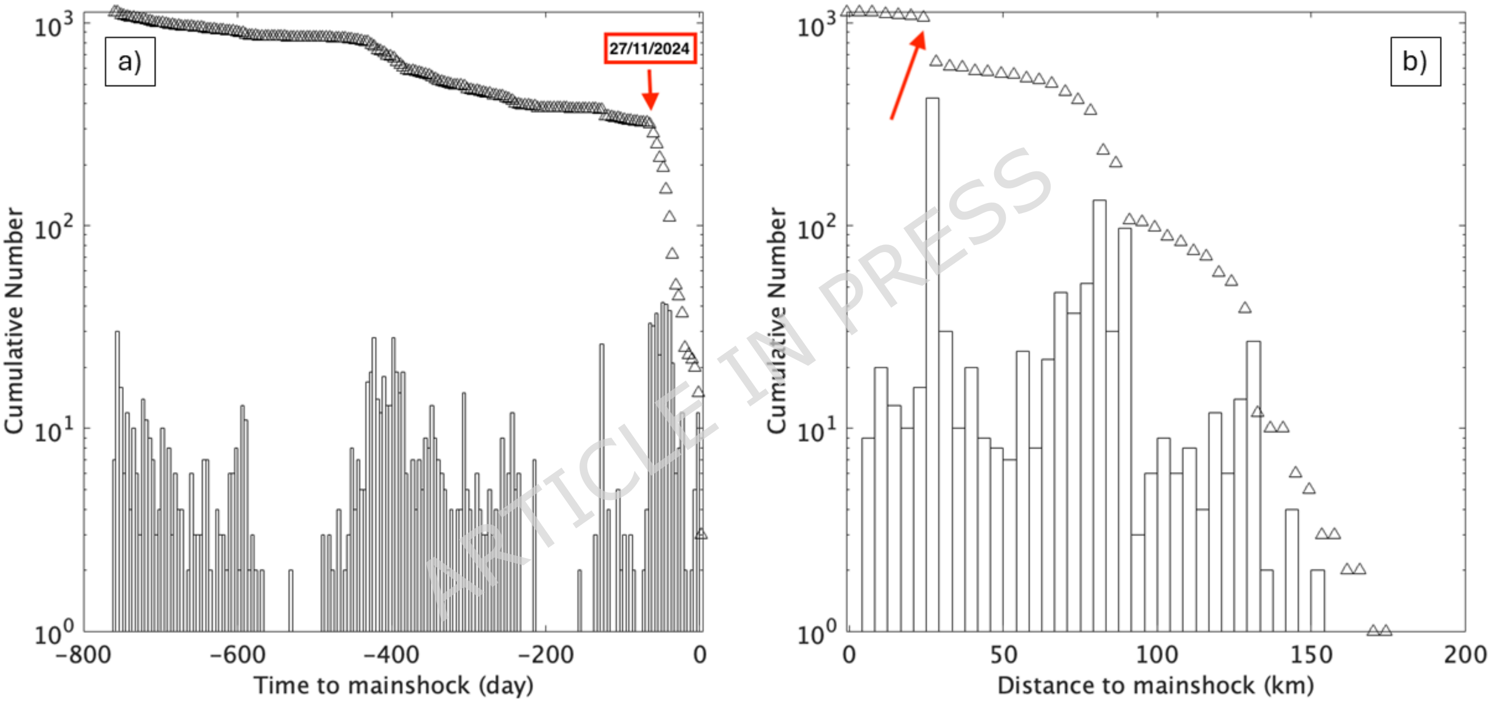
a)
27/11/2024
Cumulative Number
10^0
10^1
10^2
10^3
−800
−600
−400
−200
0
Time to mainshock (day)
b)
Cumulative Number
0
50
100
150
200
Distance to mainshock (km)

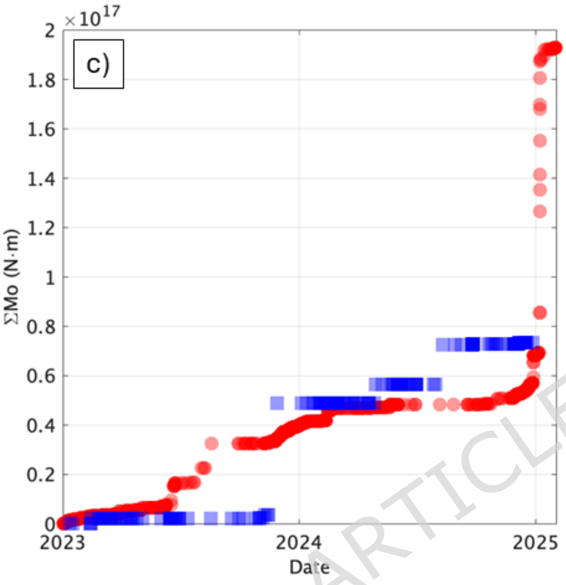
c)
×10^17
2
1.8
1.6
1.4
1.2
1
0.8
0.6
0.4
0.2
0
ΣMo (N·m)
2023
2024
2025
Date

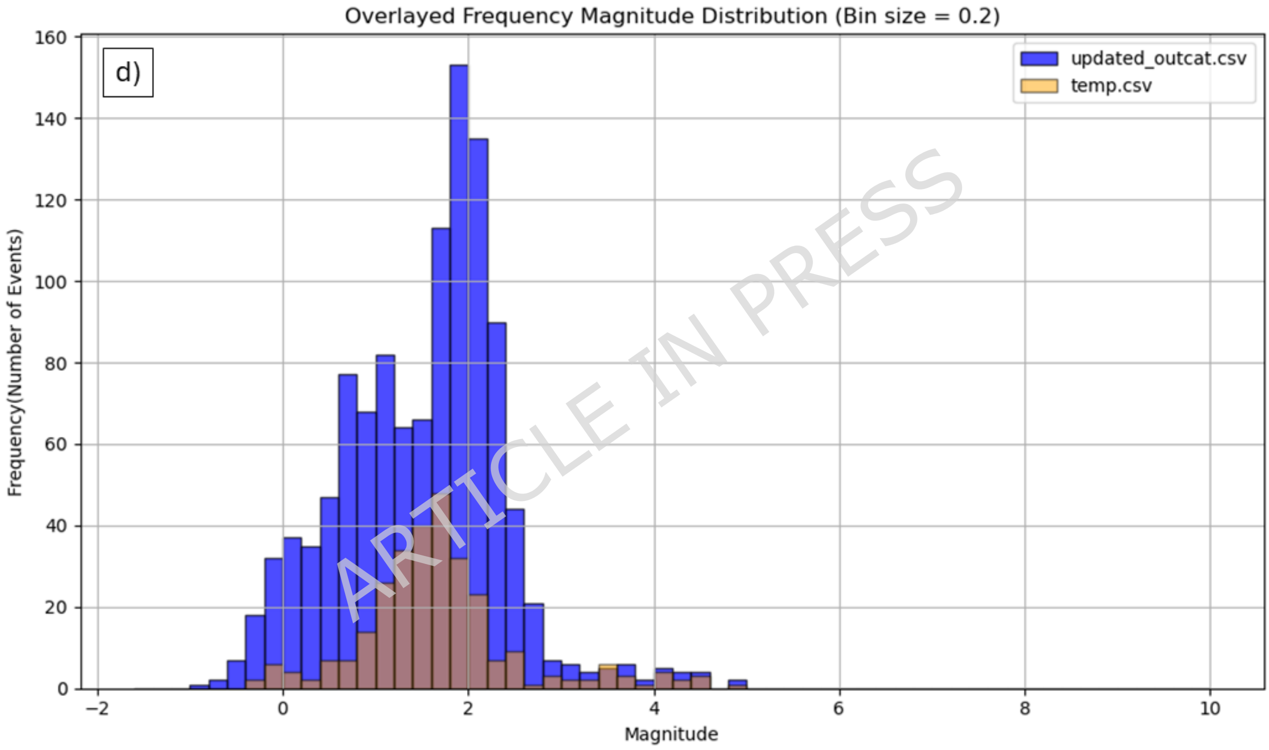
Overlayed Frequency Magnitude Distribution (Bin size = 0.2)
d)
updated_outcat.csv
temp.csv
Frequency(Number of Events)
Magnitude
0
20
40
60
80
100
120
140
160
−2
0
2
4
6
8
10

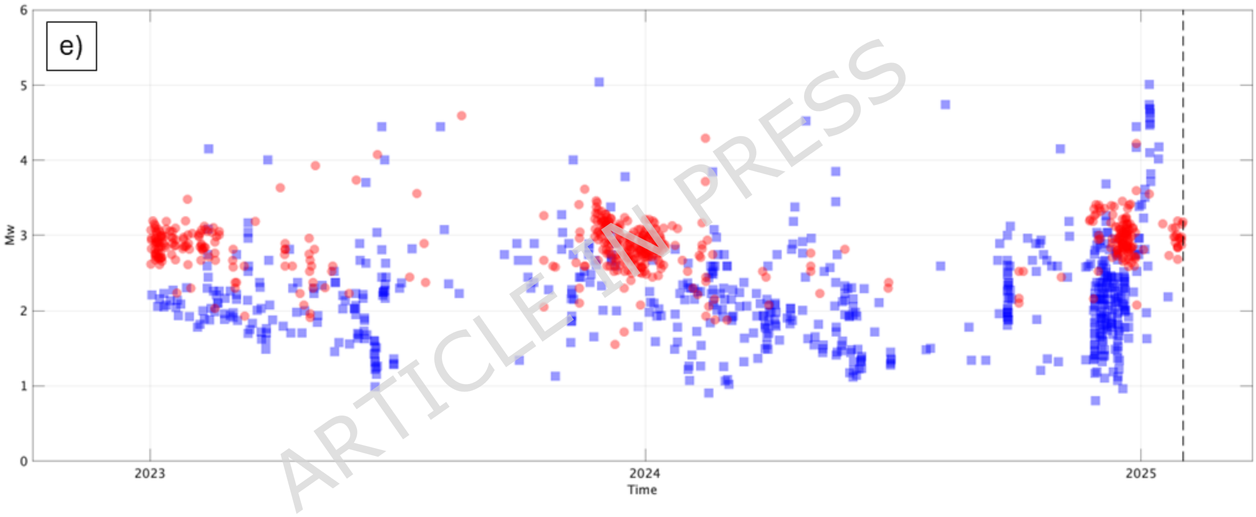
e)
Mw
6
5
4
3
2
1
0
2023
2024
2025
Time

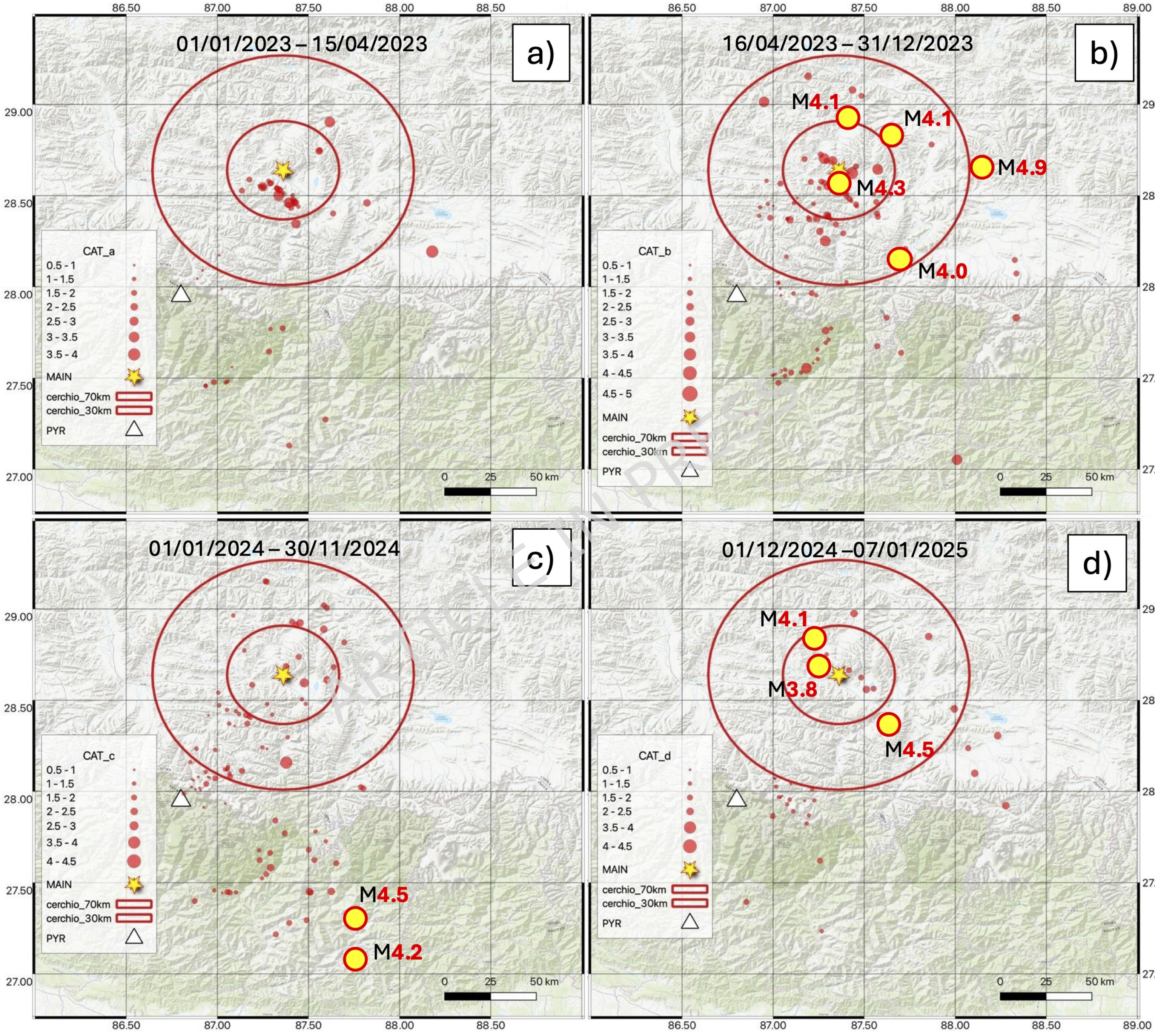
01/01/2023 – 15/04/2023
a)
16/04/2023 – 31/12/2023
b)
01/01/2024 – 30/11/2024
c)
01/12/2024 – 07/01/2025
d)
86.50
87.00
87.50
88.00
88.50
89.00
29.00
28.50
28.00
27.50
27.00
CAT_a
CAT_b
CAT_c
CAT_d
0.5 - 1
1 - 1.5
1.5 - 2
2 - 2.5
2.5 - 3
3 - 3.5
3.5 - 4
4 - 4.5
4.5 - 5
MAIN
cerchio_70km
cerchio_30km
PYR
0
25
50 km
M4.1
M4.1
M4.9
M4.3
M4.0
M4.5
M4.2
M4.1
M3.8
M4.5

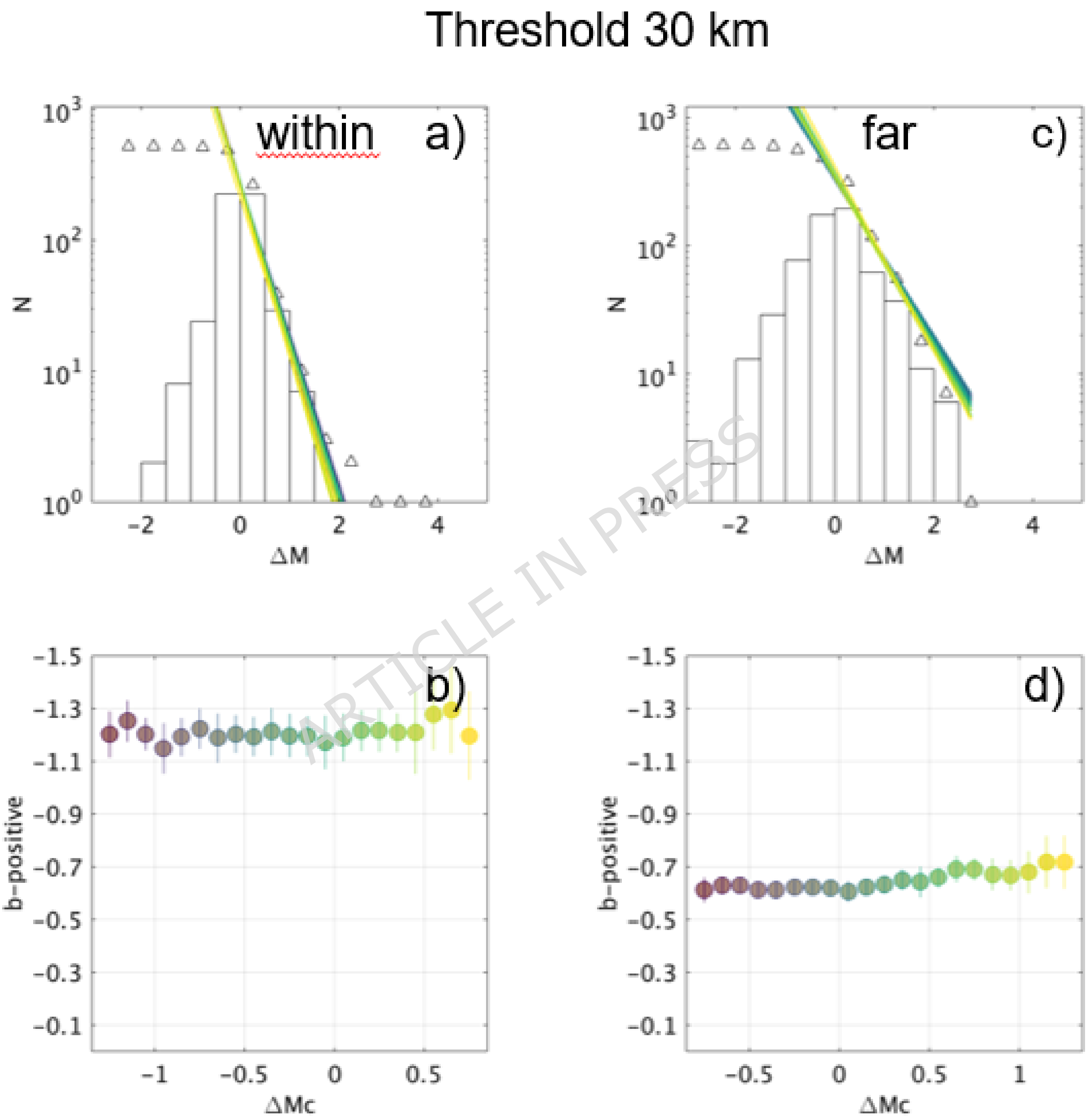
Threshold 30 km
within
a)
N
10^0
10^1
10^2
10^3
-2
0
2
4
ΔM
far
c)
N
10^0
10^1
10^2
10^3
-2
0
2
4
ΔM
b)
b-positive
-1.5
-1.3
-1.1
-0.9
-0.7
-0.5
-0.3
-0.1
-1
-0.5
0
0.5
ΔMc
d)
b-positive
-1.5
-1.3
-1.1
-0.9
-0.7
-0.5
-0.3
-0.1
-0.5
0
0.5
1
ΔMc

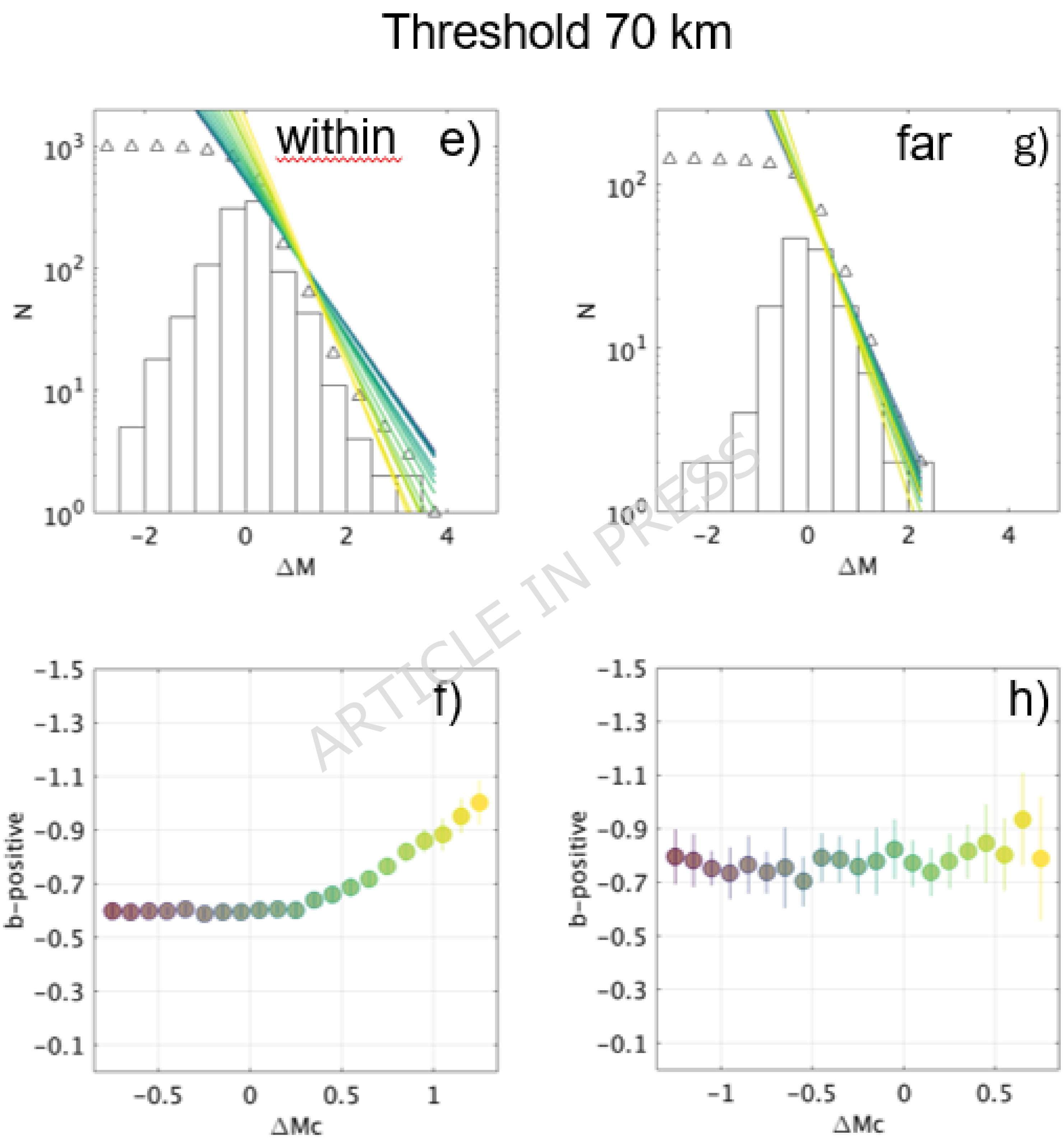
Threshold 70 km
within
e)
N
10^3
10^2
10^1
10^0
-2
0
2
4
ΔM
far
g)
N
10^2
10^1
10^0
-2
0
2
4
ΔM
f)
b-positive
-1.5
-1.3
-1.1
-0.9
-0.7
-0.5
-0.3
-0.1
-0.5
0
0.5
1
ΔMc
h)
b-positive
-1.5
-1.3
-1.1
-0.9
-0.7
-0.5
-0.3
-0.1
-1
-0.5
0
0.5
ΔMc

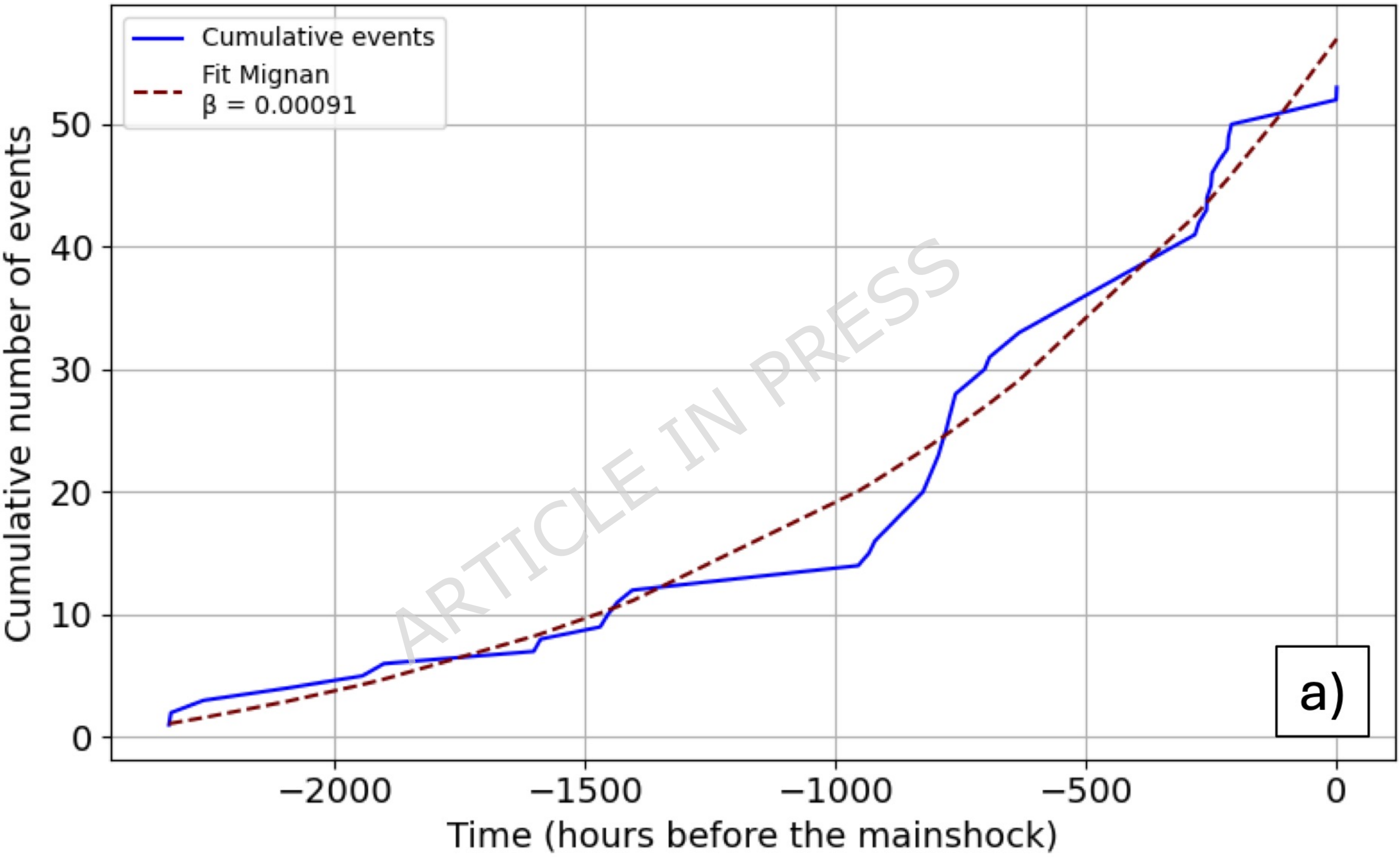
Cumulative events
Fit Mignan
β = 0.00091
Cumulative number of events
0
10
20
30
40
50
−2000
−1500
−1000
−500
0
Time (hours before the mainshock)
a)

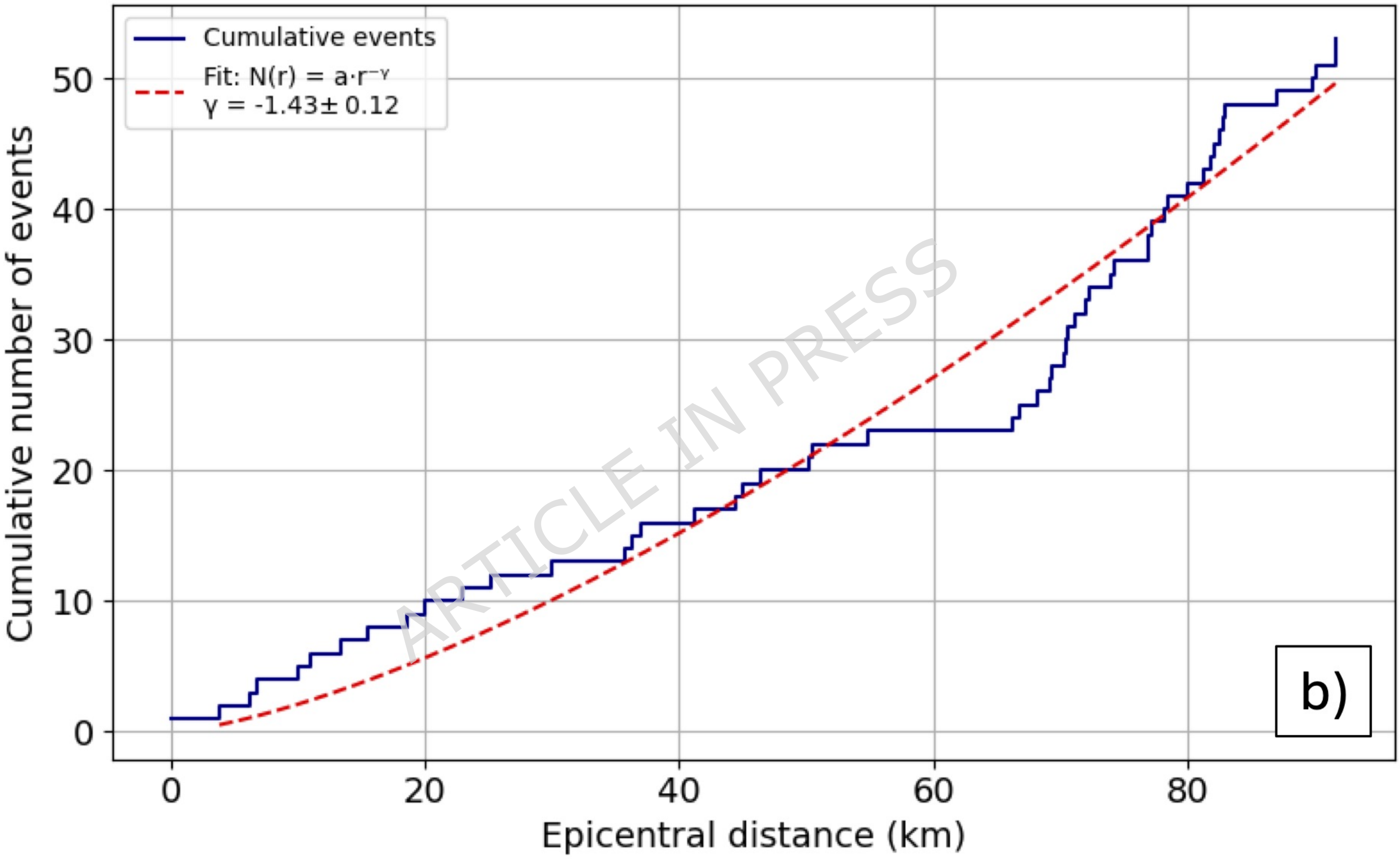
Cumulative events
Fit: N(r) = a·r⁻ᵞ
γ = -1.43± 0.12
Cumulative number of events
0
10
20
30
40
50
0
20
40
60
80
Epicentral distance (km)
b)

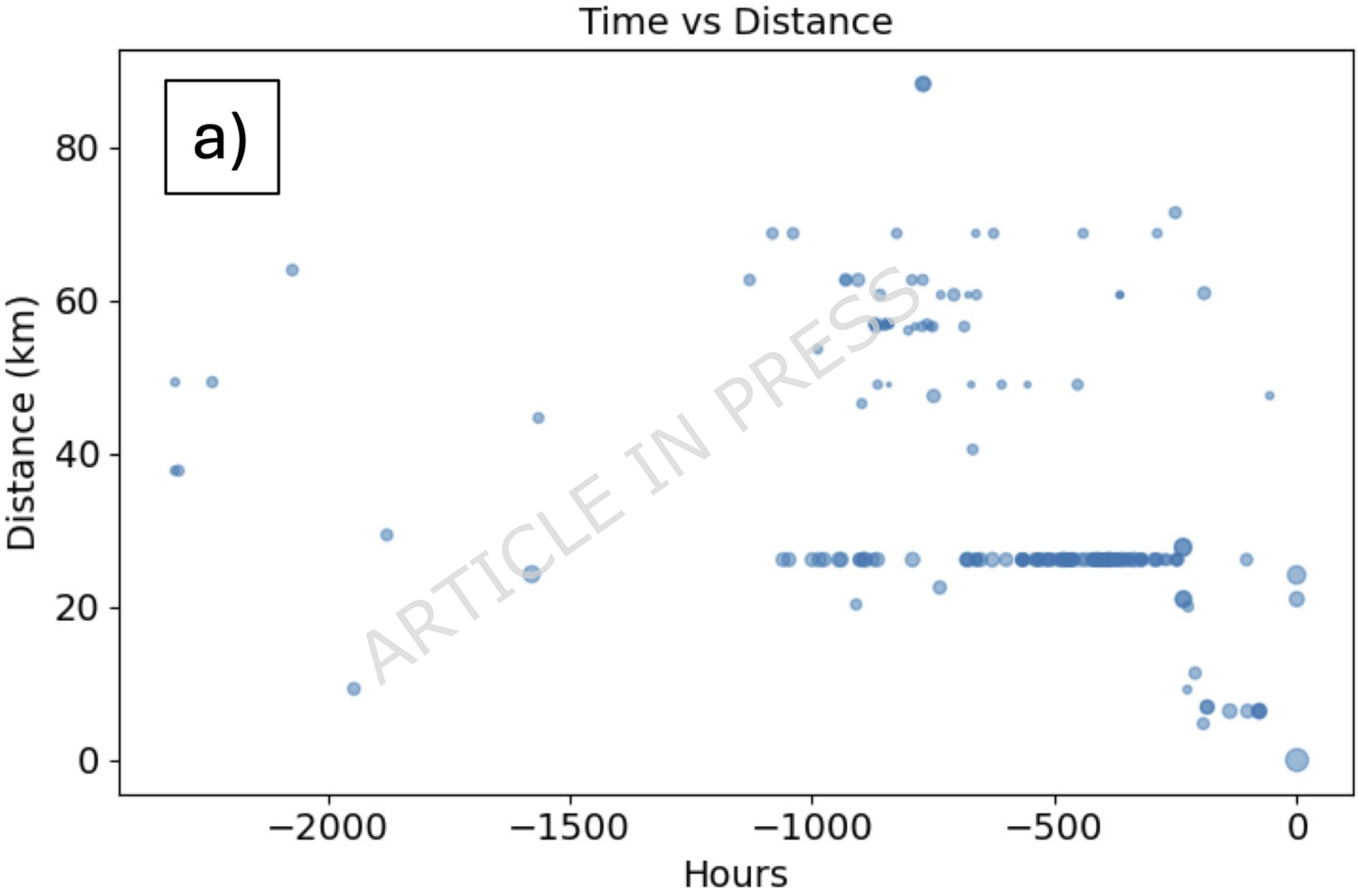
Time vs Distance
a)
Distance (km)
0
20
40
60
80
Hours
−2000
−1500
−1000
−500
0

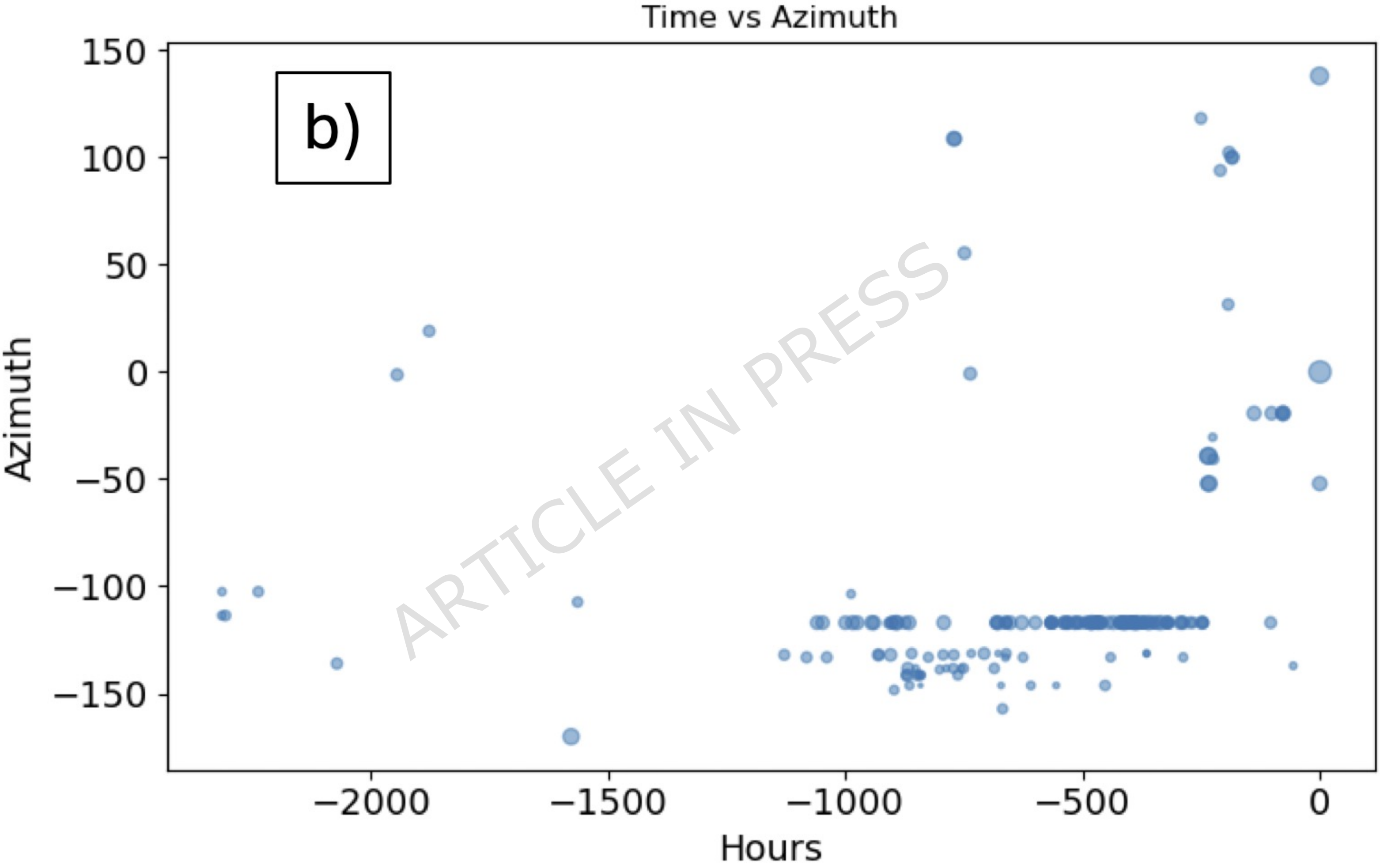
Time vs Azimuth
b)
Azimuth
150
100
50
0
−50
−100
−150
Hours
−2000
−1500
−1000
−500
0

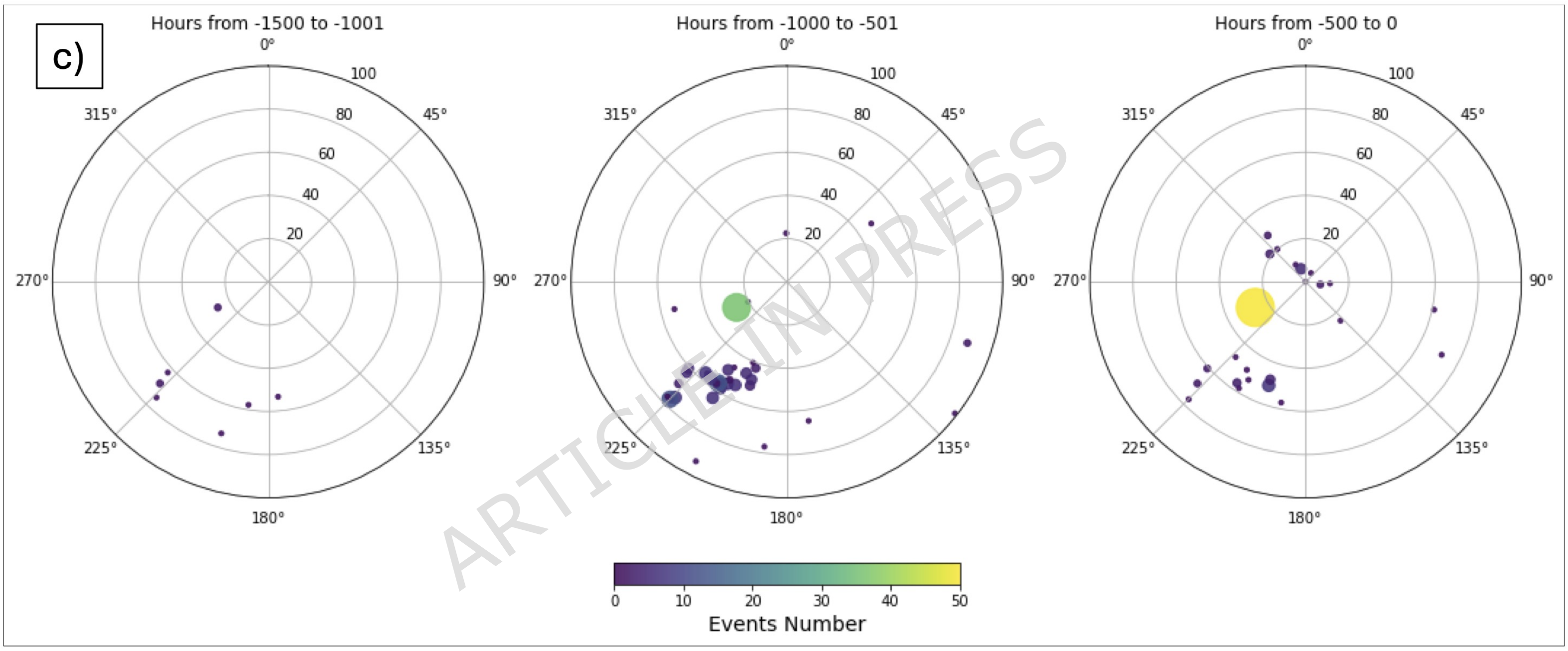
c)
Hours from -1500 to -1001
Hours from -1000 to -501
Hours from -500 to 0
0°
45°
90°
135°
180°
225°
270°
315°
20
40
60
80
100
0
10
20
30
40
50
Events Number

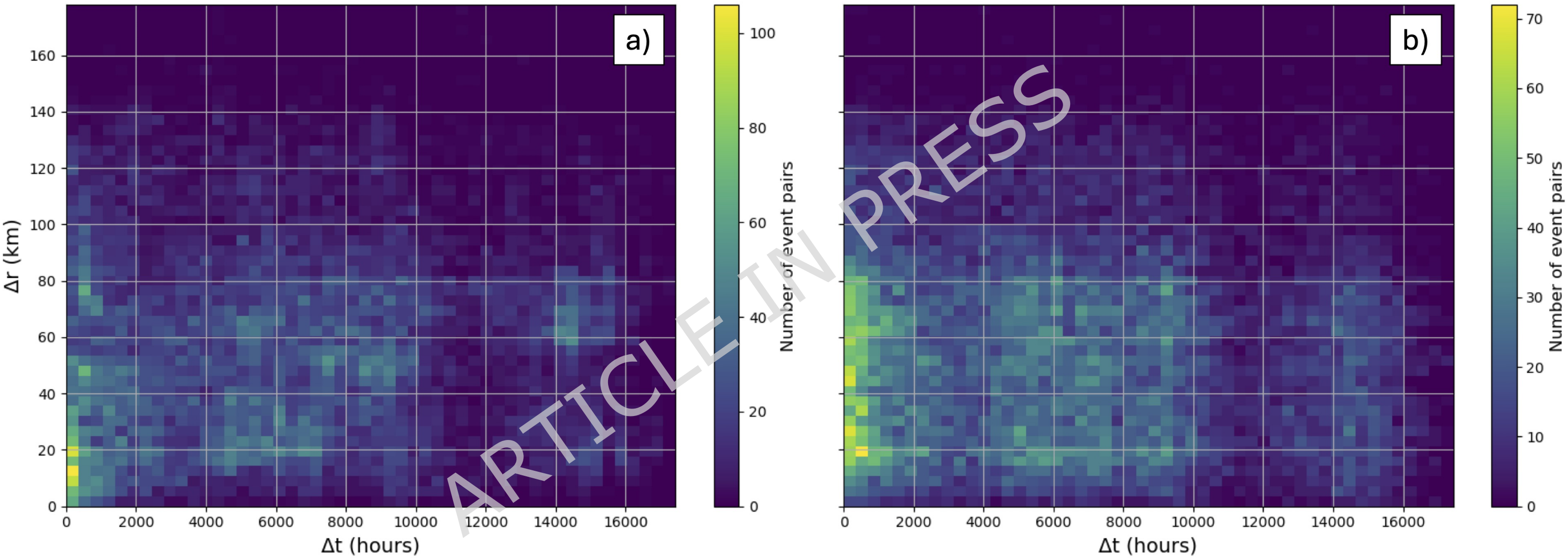
a)
b)
Δr (km)
0
20
40
60
80
100
120
140
160
Δt (hours)
0
2000
4000
6000
8000
10000
12000
14000
16000
Number of event pairs
0
20
40
60
80
100
0
10
20
30
40
50
60
70

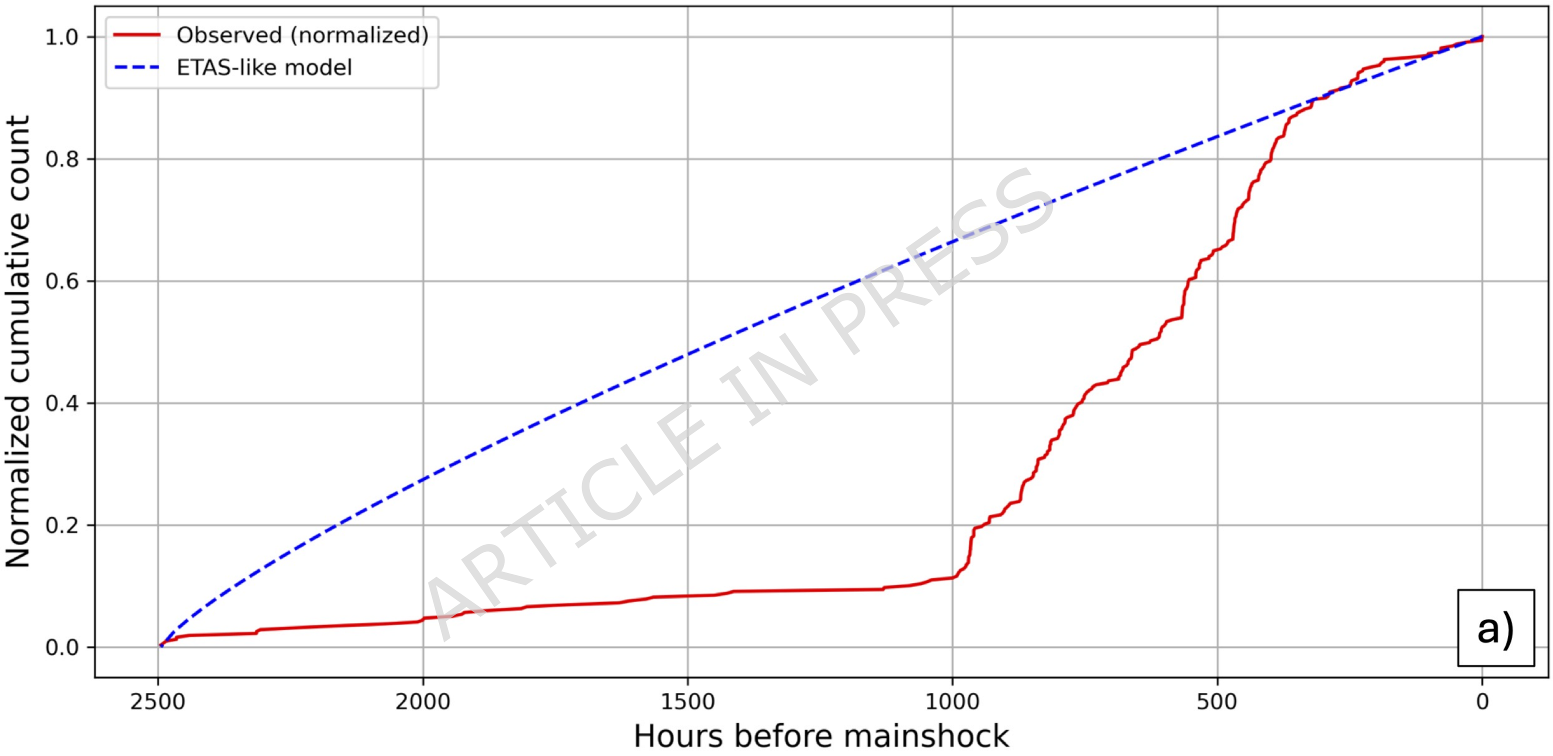
Observed (normalized)
ETAS-like model
Normalized cumulative count
1.0
0.8
0.6
0.4
0.2
0.0
2500
2000
1500
1000
500
0
Hours before mainshock
a)

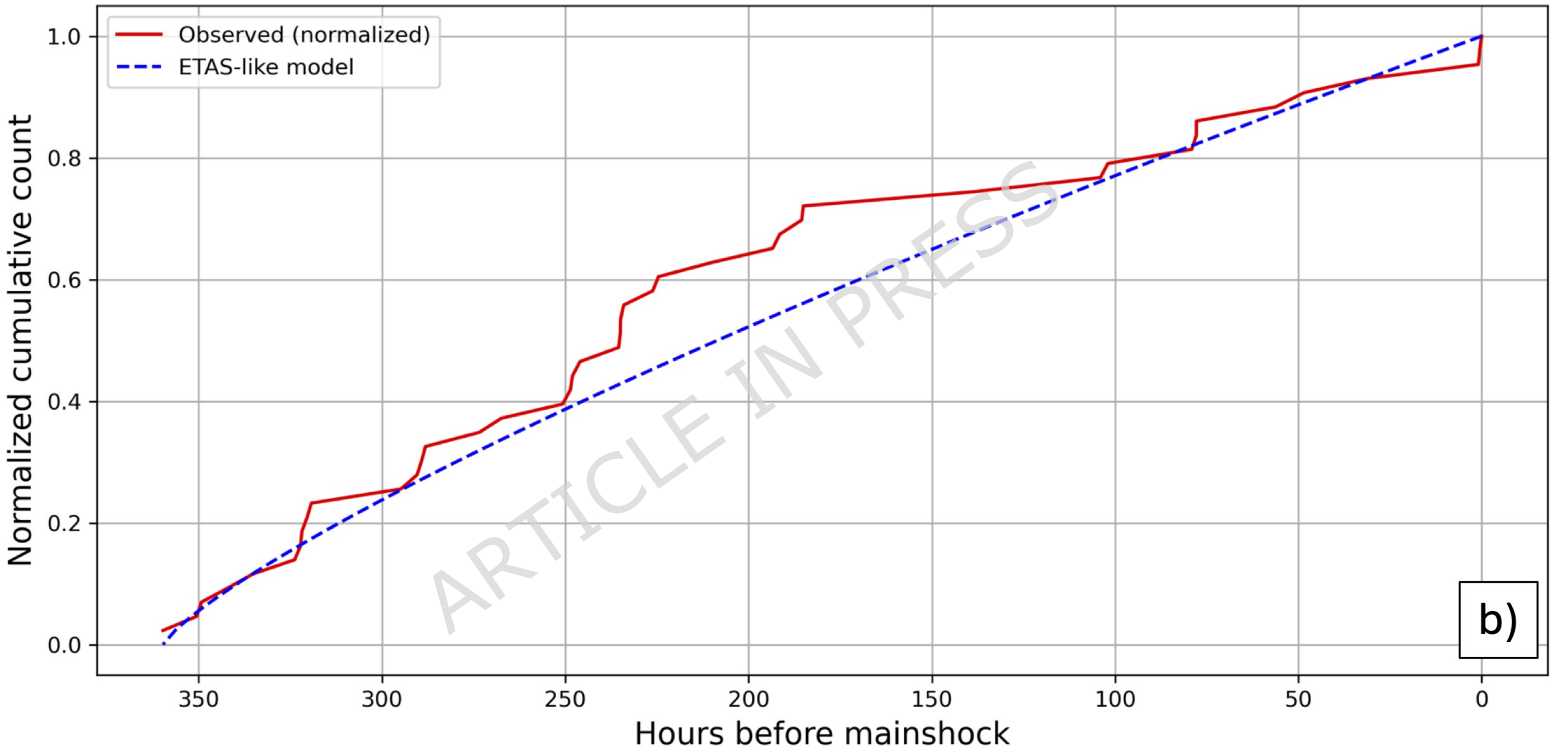
Observed (normalized)
ETAS-like model
Normalized cumulative count
0.0
0.2
0.4
0.6
0.8
1.0
Hours before mainshock
350
300
250
200
150
100
50
0
b)

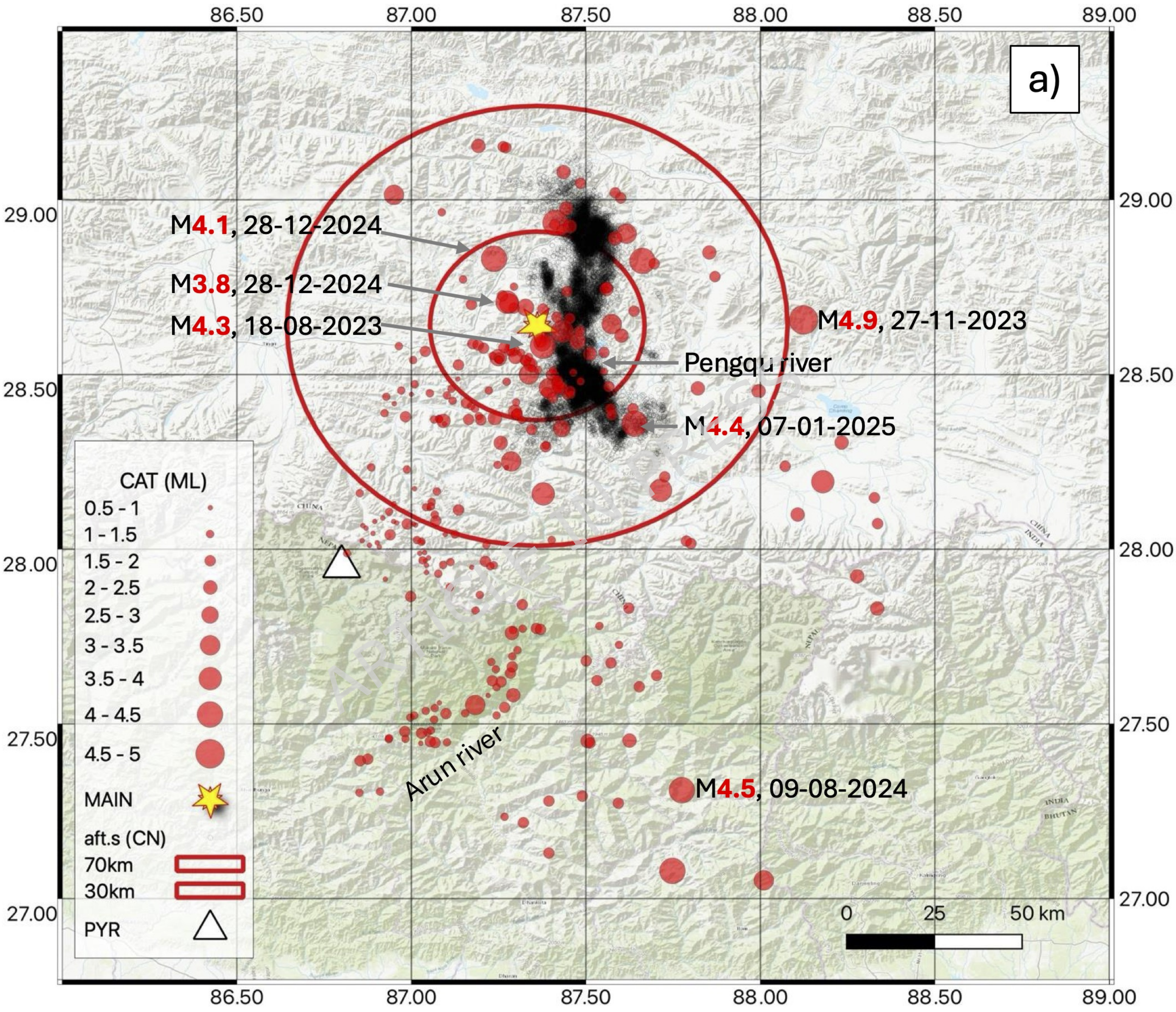
a)
86.50
87.00
87.50
88.00
88.50
89.00
29.00
28.50
28.00
27.50
27.00
M4.1, 28-12-2024
M3.8, 28-12-2024
M4.3, 18-08-2023
M4.9, 27-11-2023
Pengqu river
M4.4, 07-01-2025
M4.5, 09-08-2024
Arun river
CAT (ML)
0.5 - 1
1 - 1.5
1.5 - 2
2 - 2.5
2.5 - 3
3 - 3.5
3.5 - 4
4 - 4.5
4.5 - 5
MAIN
aft.s (CN)
70km
30km
PYR
0
25
50 km

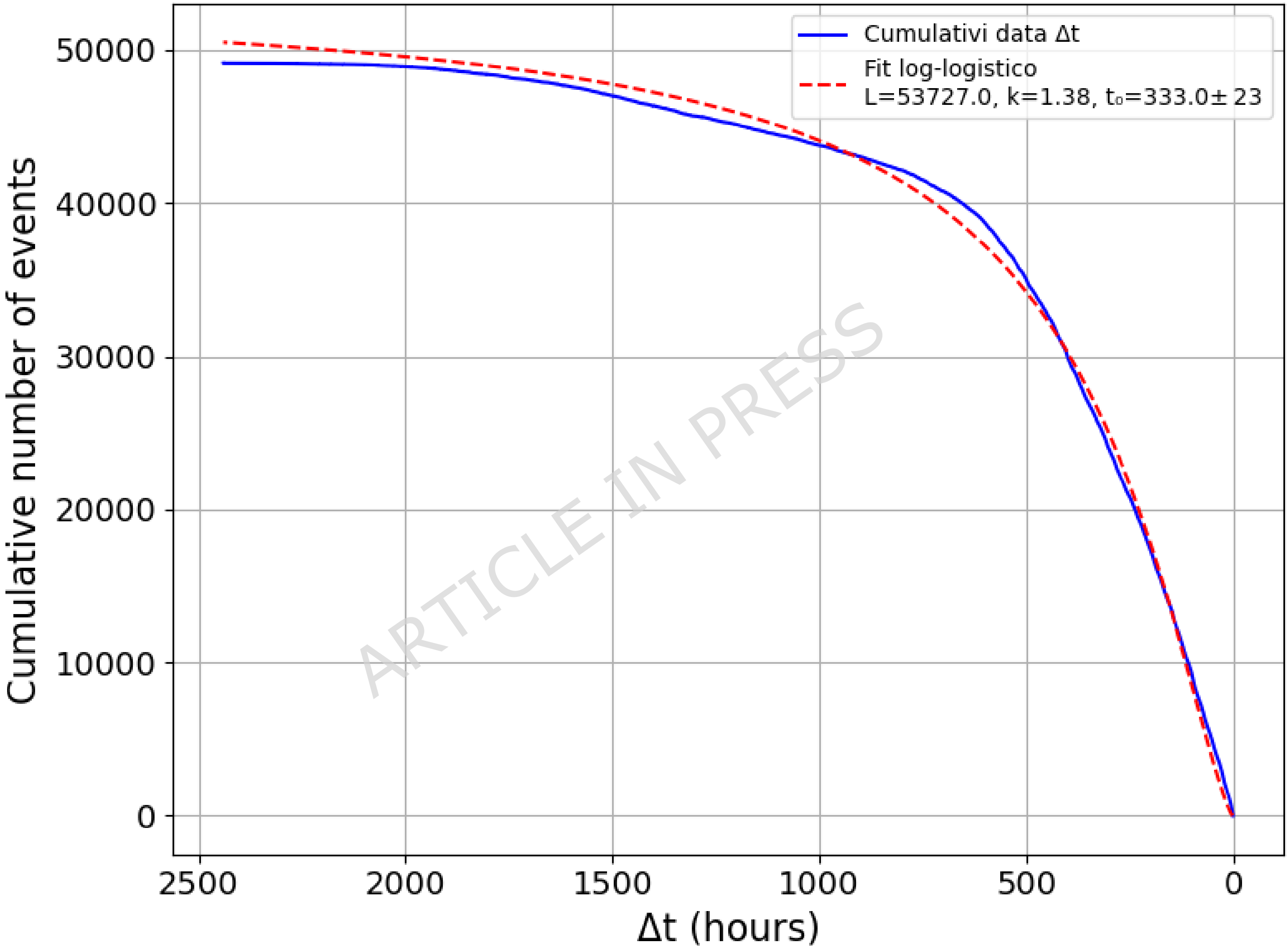
Cumulativi data Δt
Fit log-logistico
L=53727.0, k=1.38, t₀=333.0± 23
Cumulative number of events
50000
40000
30000
20000
10000
0
2500
2000
1500
1000
500
0
Δt (hours)

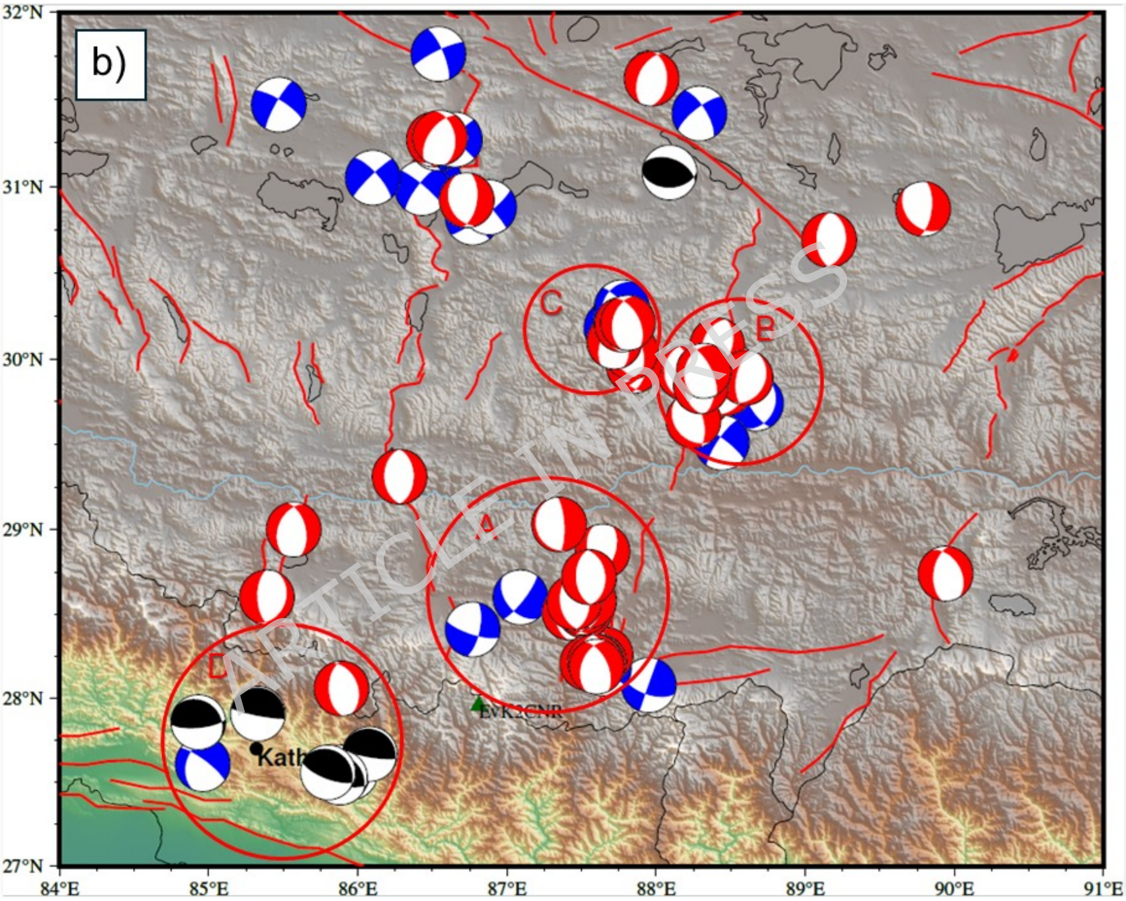
b)
C
B
A
D
Kath
EVK2CNR
32°N
31°N
30°N
29°N
28°N
27°N
84°E
85°E
86°E
87°E
88°E
89°E
90°E
91°E

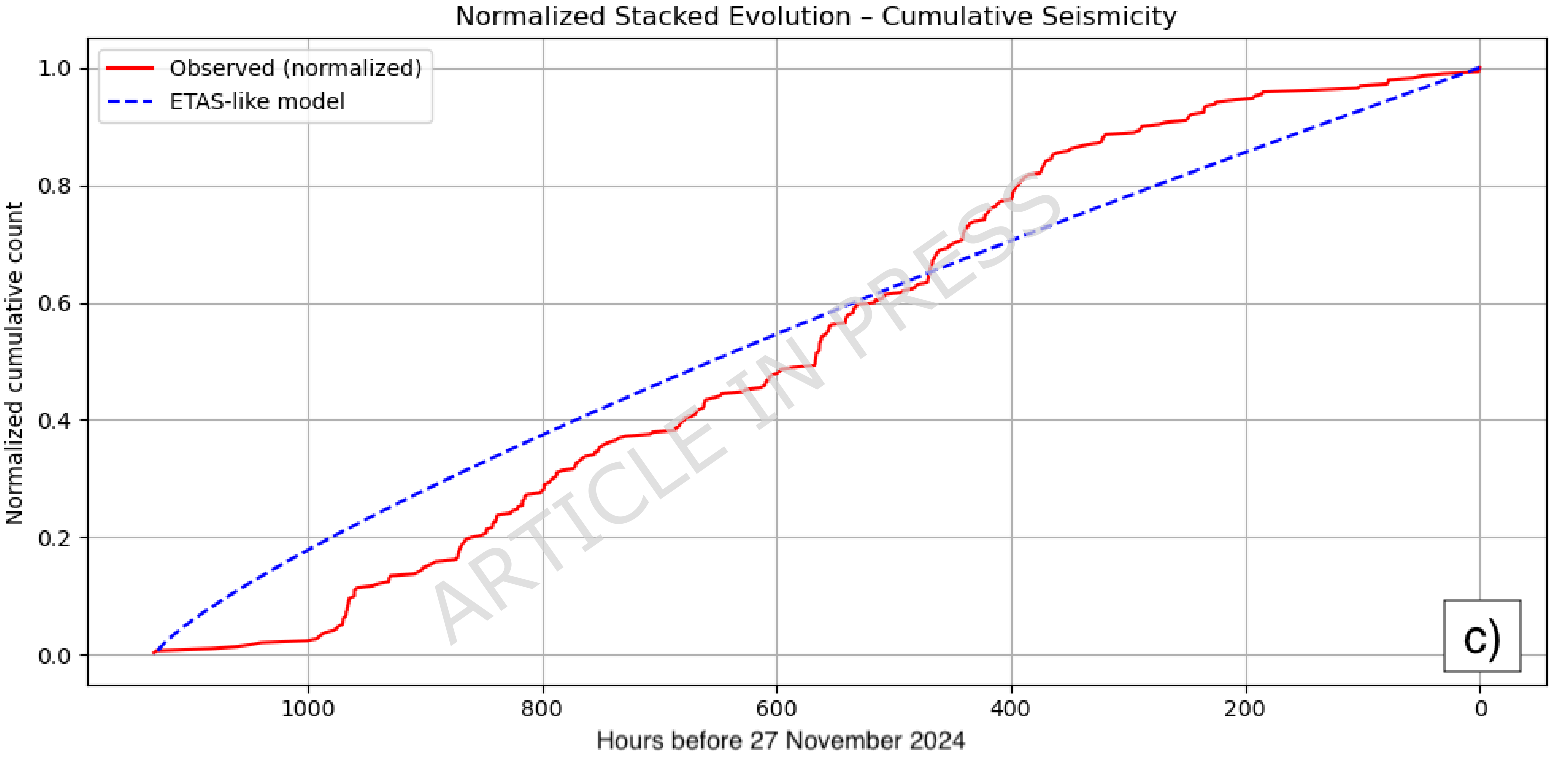
Normalized Stacked Evolution – Cumulative Seismicity
Observed (normalized)
ETAS-like model
Normalized cumulative count
1.0
0.8
0.6
0.4
0.2
0.0
1000
800
600
400
200
0
Hours before 27 November 2024
c)